International Journal of Heat and Mass Transfer 191 (2022) 122837

Contents lists available at ScienceDirect

International Journal of Heat and Mass Transfer

journal homepage: www.elsevier.com/locate/hmt

# Bouncing modes and heat transfer of a dielectric droplet in the presence of an external electric field

R. Deepak Selvakumar[a], Hyoungsoon Lee[a,b,*]

[a] School of Mechanical Engineering, Chung-Ang University, Seoul 06974, South Korea
[b] Department of Intelligent Energy and Industry, Chung-Ang University, Seoul 06974, South Korea

ARTICLE INFO

*Article history:*
Received 12 January 2022
Revised 28 February 2022
Accepted 18 March 2022

*Keywords:*
Electrohydrodynamics
Heat transfer
Single droplet
Bouncing dynamics
Thermal management

ABSTRACT

A numerical investigation of droplet bouncing and heat transfer over a heated surface in the presence of an external electric field has been reported. The coupled set of governing equations including the electrostatic and incompressible Navier-Stokes equations, have been implemented in the finite-volume framework of OpenFOAM®. The coupled level set and volume of fluid (CLSVOF) approach has been used to capture the droplet interface. The influence of the electric field over the droplet dynamics and bouncing modes are systematically studied. Different bouncing modes are observed and they have been mapped with respect to the electric capillary number, $Ca_E$ and Weber number, $We$. Two new modes have been identified at $Ca_E = 0.1$. The Coulombic attraction at the solid-liquid contact line extends the total contact time of the droplet. The local electric field distribution depends on the droplet's local curvature. The stronger distribution of electrostatic pressure near the tip of the droplet induces a stretching behavior. The stretched droplet, extended contact time and enhanced fluid circulation increase the heat transfer. This work provides a deeper understanding of droplet impact, bouncing dynamics and related heat transfer characteristics influenced by an external electric field.



## 1. Introduction

Heat transfer using a liquid spray is a common technique to dissipate heat in several applications such as quenching of metal casting [1], exhaust gas treatment systems [2,3] and electronic cooling [4], etc. Recently, electrohydrodynamic (EHD) flow induced heat transfer enhancement is popular among researchers due to its quick response, low power consumption and design flexibility with no moving parts [5]. Electrospray cooling is being considered as an alternative to the conventional spray cooling due to its advantages such as better atomization processes, superior droplet size control, better droplet speed control, and higher efficiency than mechanical pumps [6]. Several investigations are reported in the literature on overall heat transfer performance of electrospray cooling systems [7,8]. But, very limited information is available on the dynamics of a single droplet impact and corresponding heat transfer over a hot surface in the presence of an electric field. Coupled interaction of the electric field with the flow and thermal fields make the droplet dynamics and related heat transfer processes more complex and intricate. Given its practical relevance and complex nature, droplet bouncing dynamics under the combined actions of inertial force, surface tension, thermal buoyancy and electric field have become a problem of academic and research interest. Deeper insights on this problem will help to design electrospray cooling systems with improved cooling efficiency. In addition to heat transfer characteristics of electrospray cooling systems, the droplet impact dynamics in the presence of an electric field has applications in other industrial processes such as emulsification [9,10], drug development [11,12], lab-on-chip processes involving biochemical agents [13], ink-jet printing [14], and droplet-based microfluidic processes [15].

In general, when a droplet impacts a flat solid surface, it will first spread on the surface due to its inertia. After spreading, the droplet will retract back due to the surface tension. Retraction is followed by upward stretching of the droplet tip. Finally, the droplet rebounds or splashes [16,17]. The impact and bouncing dynamics of the droplet are different in the presence of an external electric field. For instance, the electrostatic force tends to make the droplet tip to become very sharp. Thus, the local electric field gets distorted and might lead to a flash-over or corona discharge [18–21], affecting the safety of the device and system. To avoid these harmful effects, a deeper understanding of droplet dynamics in the presence of electric field is very important. Experimental and numerical investigations on the effect of droplet deformation on the

* Corresponding author.
*E-mail address:* leeh@cau.ac.kr (H. Lee).
*URL:* http://atsla.cau.ac.kr (H. Lee)

https://doi.org/10.1016/j.ijheatmasstransfer.2022.122837

**Nomenclature**

| | |
|---|---|
| $L_H$ | Height of the domain [m]. |
| $L_W$ | Width of the domain [m]. |
| $D$ | Diameter of the droplet [m]. |
| $V$ | Electric potential [V]. |
| $\overrightarrow{E}$ | Electric field [$Vm^{-1}$]. |
| $U$ | Absolute velocity [$ms^{-1}$]. |
| $\overrightarrow{u}$ | Velocity vector [$ms^{-1}$]. |
| $p$ | Pressure [$kgm^{-1}s^{-2}$]. |
| $\overrightarrow{g}$ | Acceleration due to gravity [$ms^{-2}$]. |
| $C_p$ | Specific heat capacity [$Jkg^{-1}K^{-1}$]. |
| $q$ | Charge density [$Cm^{-3}$]. |
| $K$ | Electric conductivity [$Sm^{-1}$]. |
| $We$ | Weber number. |
| $Ca_E$ | Electric capillary number. |
| $Ra$ | Rayleigh number. |
| $Pr$ | Prandtl number. |
| $k$ | Thermal conductivity [$Wm^{-1}K{-}1$]. |
| $t$ | Time [s]. |
| $H$ | Heaviside function. |
| $\psi$ | Ionic diffusivity [$m^2s^{-1}$]. |
| $\alpha_T$ | Thermal diffusivity [$m^2s^{-1}$]. |
| $\theta$ | Temperature [K]. |
| $\rho$ | Density [kg $m^{-3}$]. |
| $\alpha$ | Phase/Volume fraction. |
| $\xi$ | Expansion coefficient [$K^{-1}$]. |
| $\sigma$ | Surface tension [$Nm^{-1}$]. |
| $\varepsilon$ | Dielectric permittivity [$Fm^{-1}$]. |
| $\nu$ | Kinematic viscosity [$m^2s^{-1}$]. |
| $\beta$ | Spreading factor. |
| $\phi$ | Level set function. |
| $\delta$ | Dirac function. |
| $\eta$ | Pressure ratio. |
| $W, S$ | Value over the solid surface. |
| $\infty$ | Ambient/Far stream value. |
| 0 | Initial value. |
| 1, 2 | Fluid 1 (droplet) and 2 (gas). |
| $max$ | Maximum value. |
| $*$ | Non-dimensional value. |
| $M$, $L$ | Mean and local value. |
| $R$ | Ratio. |

contact charge process of a neutral droplet over a flat electrode were carried out by Khorsidi et al. [22]. A three step charging process of a water droplet over a charged flat electrode surface was experimentally demonstrated by Im et al. [23]. Likewise, Bormanshenko et al. [24,25] experimentally studied the deformation behavior of smoothly deposited droplets over a super-hydrophobic surface in the presence of a vertical electric field. They studied the electrowetting behavior of charged droplets. It was observed that the charged droplets exhibited deformation from their natural shape and also a different wetting behavior. Majority of the studies concentrate on the contact charge process, rather than the dynamic impact behavior [26].

The droplet dynamics after impact in the presence of an electric field is decided by the competition between surface tension and electrostatic forces. In this context, an experimental study by Ryu and Lee [27] investigated the spreading behavior of charged and neutral droplets on impact over a hydrophobic surface. The charged droplet showed higher maximum spreading diameter than the neutral droplet. The wetting characteristics of a dielectric droplet impacting over a solid surface was numerically investigated by Pal et al. [28] and Yurkiv et al. [29]. It was concluded that an electric field could be employed to develop surfaces with tunable wetting features. A numerical study on droplet impact on a surface under an electric field by Emdadi and Pournaderi [30] showed that the electric field led to longer contact times of the droplet. These studies have only reported the droplet deformation and bouncing during impact of a dielectric droplet over a solid surface in the presence of an electric field. However, the droplet stretching in the upward direction after retraction might cause distortion in local electric field distribution. This can lead to enhanced electrostatic force near the tip leading to stretching and ejection behavior, synonymous to a cone-jet mode [31]. Recently, Tian et al. [32] experimentally demonstrated the droplet stretching behavior after impact over a solid surface in the presence of a vertical electric field and reported two new droplet breakup and stretching modes.

The droplet stretching behavior in the presence of electric field deserves further systematic investigation. In addition, the droplet impact dynamics over a heated surface in the presence of an external electric field is yet to be studied. The combined interactions of fluid flow, thermal, and electric fields are expected to cause shifts and modifications in the bouncing modes of the droplet. This study presents a detailed numerical investigation of bouncing and heat transfer characteristics of a dielectric droplet over a heated hydrophobic surface in the presence of an external electric field. The different dynamic modes observed at various Weber numbers ($We$) and electric capillary numbers ($Ca_E$) are mapped. The heat transfer characteristics during the stretching mode is quantified. The present study provides useful insights into the mechanism of droplet impact dynamics in the presence of electric field and the related heat transfer characteristics. Our study will serve as a guide for the development of engineering systems that involve electric field, droplet dynamics and heat transfer.

## 2. Mathematical formulation

This section presents the physical description of the problem, governing equations of the numerical model, boundary conditions and non-dimensional parameters used for the analysis.

### 2.1. Problem description

An axisymmetric computational domain with height $L_H$ and width $L_W$ is considered, as shown in Fig. 1. The left boundary of the domain is considered as the axis of symmetry. The bottom wall is maintained at a temperature $\theta_W$ higher than the ambient temperature $\theta_\infty$. All the other boundaries, except the bottom wall are kept at ambient temperature $\theta_\infty$. The top boundary is considered the high voltage electrode and the bottom boundary is grounded. The applied electric potential between the electrodes is $\Delta V$. Thus, the electric field $\overrightarrow{E}$ acts in a vertically downward direction. A spherical leaky dielectric droplet of diameter $D_0$ at ambient temperature $\theta_\infty$ impacts the hot bottom wall, with an absolute initial velocity $U_0$. Detailed information about the boundary condition is presented in Table 1.

### 2.2. Governing equations

A two-phase electrothermohydrodynamic (ETHD) model for two immiscible, incompressible, Newtonian fluids based on coupled level set and volume of fluid (CLSVOF) method has been adopted. The coupled set of governing equations include the continuity and momentum equations for the fluid flow, energy equation for the thermal transport, interface capturing advection equation, Poisson equation for electric potential and charge conservation equation.

$$\nabla.\overrightarrow{u} = 0 \quad (1)$$

**Table 1**
Boundary conditions.

| | Top $y=H$ | Bottom $y=0$ | Right $x=L_W$ | Axis $x=0$ |
|---|---|---|---|---|
| Pressure $p$ | $\nabla p=0$ | $\nabla p=0$ | Total pressure | Symmetry |
| Velocity $\vec{u}$ | $\nabla\vec{u}=0$ | $\vec{u}=0$ | $\nabla\vec{u}=0$ | Symmetry |
| Charge density $q$ | $\nabla q=0$ | $\nabla q=0$ | $\nabla q=0$ | Symmetry |
| Electric potential $V$ | $V=V_0$ | $V=0$ | $\nabla V=0$ | Symmetry |
| Volume fraction $\alpha$ | Inlet-Oulet | Constant Contact Angle | Inlet-Outlet | Symmetry |
| Temperature $\theta$ | $\theta=\theta_\infty$ | $\theta=\theta_W$ | $\theta=\theta_\infty$ | $\theta=\theta_\infty$ |

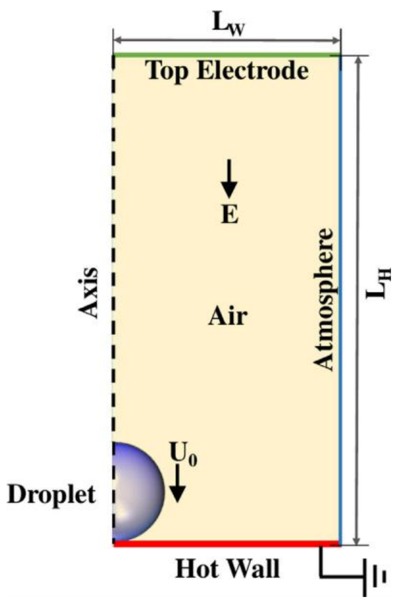


**Fig. 1.** Schematic representation of the computational domain.

$$\frac{\partial \rho \vec{u}}{\partial t}+\nabla.\left(\rho\vec{u}\,\vec{u}\right)=-\nabla p+\rho\vec{g}+\nabla.\left[\mu\left(\nabla\vec{u}+\vec{u}^{T}\right)\right]+\mathbf{F}_{st}+\mathbf{F}_{es} \tag{2}$$

$$\frac{\partial \rho C_p\theta}{\partial t}+\nabla.\left[\rho C_p\vec{u}\,\theta\right]=\nabla.(\alpha_T.\nabla\theta) \tag{3}$$

$$\frac{\partial \alpha}{\partial t}+\nabla.\left(\alpha\vec{u}\right)=0 \tag{4}$$

Here $\vec{u}$ is the velocity vector, $\vec{g}$ is the acceleration due to gravity, $p$ is the pressure and $\theta$ is the temperature. The buoyancy source term $\rho\vec{g}$ is calculated using the Boussinesq approximation. In dielectric fluids, the Joule heating effect results in very low variation in temperature $(1\times10^{-4}Ks^{-1})$. Thus, Joule heating effects are generally neglected in electrohydrodynamics of dielectric fluids [29,32–35]. The terms $\mathbf{F}_{st}$ and $\mathbf{F}_{es}$ represent the volumetric source terms due to surface tension and electric field, respectively. The phase fraction in each control volume is denoted by $\alpha$ and the advection equation for the phase fraction is solved explicitly to capture the droplet interface movement.

*2.2.1. Coupled level set and volume of fluid (CLSVOF) approach*

The CLSVOF approach employed in this study guarantees the mass conservation of volume of fluid (VOF) method and accurate interface capturing of the level set (LS) approach. The solution of dedicating fully conserved scalar advection equation for the phase fraction ensures that mass is conserved. Whereas, the simultaneous coupling of LS function $\phi$ ensures smoothness of the solution across the interface and permits the use of simple finite differencing schemes to compute normal vector and interface curvature. This helps us to capture a sharp interface without any nonphysical oscillations across the interface, while also ensuring mass conservation. The value of LS initialized from the VOF phase fraction scalar field and the interface position is considered along the contour line $\alpha = 0.5$.

$$\phi_0=(2\alpha-1)\Gamma \tag{5}$$

Here, $\Gamma$ is a non-dimensional parameter that decides the numerical stability and accuracy. Large values of $\Gamma$ result in numerical instability and small values will lead to inaccurate results. As a general practice, the value of $\Gamma$ is decided based on the local grid size as $\Gamma=0.75|\Delta x|$ [36]. The initial value $\phi_0$ is a sign function with a value above zero in the liquid droplet region and less than zero in the ambient gaseous region. The variable $\phi$ is then re-distanced by the re-initialization equation as follows [37] :

$$\begin{cases}\frac{\partial\phi}{\partial\tau}=sgn(\phi_0)(1-\nabla\phi)\\ \phi(x,0)=\phi_0(x)\end{cases} \tag{6}$$

$\tau=0.1\Delta x$ is a pseudo-time and $sgn(\phi_0)$ is a sign function. The re-initialization of smoothing level-set function achieves convergence within a few iterations, where the iteration number $\phi_{corr}=h/\Delta\tau$. $h = 1.5\Delta x$ is the interface thickness [38].

The volumetric source term indicating the interfacial surface tension force $\vec{F}_{st}$ in Eq. (2) is computed according to the continuum surface model [39], as follows:

$$\vec{F}_{st}=\sigma\kappa(\phi)\delta(\phi)\nabla(\phi) \tag{7}$$

where $\sigma$ is the surface tension and the interface curvature $\kappa(\phi)$ is calculated as

$$\kappa(\phi)=-\nabla.\left(\mathbf{n}.\mathbf{S}_f\right) \tag{8}$$

In Eq. (8), $\mathbf{S}_f$ is the surface vector of the cell face and the unit normal vector $\mathbf{n}$ is determined as

$$\mathbf{n}=\frac{\delta\phi}{|\delta\phi|} \tag{9}$$

The Dirac function $\delta(\phi)$ that limits the influence of interfacial tension within the interface is defined as

$$\delta(\phi)=\begin{cases}0 & if\ |\phi|\ >\ h\\ \frac{1}{2h}\left(1+\cos\left(\frac{\pi\phi}{h}\right)\right) & if\ |\phi|\ \le\ h\end{cases} \tag{10}$$

The density, viscosity and specific heat capacity are calculated as a function of LS variable as

$$\rho(\phi)=\rho_1H(\phi)+\rho_2(1-H(\phi)) \tag{11}$$

$$\mu(\phi)=\mu_1H(\phi)+\mu_2(1-H(\phi)) \tag{12}$$

$$C_p(\phi)=C_{p1}H(\phi)+C_{p2}(1-H(\phi)) \tag{13}$$

where, $H(\phi)$ is the Heaviside function:

$$H(\phi)=\begin{cases}0 & if\ \phi\ <-h\\ \frac{1}{2}\left(1+\frac{\phi}{h}+\frac{1}{\pi}\sin\left(\frac{\pi\phi}{h}\right)\right) & if\ |\phi|\ \le\ h\\ 1 & if\ \phi\ >\ h\end{cases} \tag{14}$$

The subscripts '1' and '2' denote the droplet (fluid 1) and surrounding gaseous phase (fluid 2), respectively.

### 2.2.2. Electrostatic and charge transport model

Present study considers the coupling of electrostatics and hydrodynamics by means of the source term $\mathbf{F}_{es}$ in Eq. (2). The electrostatic body force $\mathbf{F}_{es}$ is calculated using the Korteweg-Helmoholtz formula [40] as follows:

$$\mathbf{F}_{es}=\nabla.\mathbf{T}=q\vec{E}-\frac{1}{2}|E|^2\nabla\varepsilon \tag{15}$$

where, $q$ is the volumetric charge density, $\varepsilon$ denotes the dielectric permittivity and $\vec{E}$ is the electric field.

Present study considers a droplet of de-ionised (DI) water surrounded by air. Air is considered a perfect dielectric fluid [41] and DI water is a leaky dielectric material [41,42]. This can also be established based on the charge relaxation and hydrodynamic characteristic times [29,32,43,44]. The electric relaxation time $t_e=\varepsilon/K$ in droplet is $1.29e^{-4}s$. The hydrodynamic characteristic time in droplet $t_h=\rho l^2/\mu$ is $0.27e^0 s$. The charge relaxation and hydrodynamic characteristic times for air are $7.37s$ and $0.021s$, respectively. We can clearly see that $t_e<<t_h$ for DI water and $t_e>>t_h$ for air. Thus, present study deals with a leaky dielectric droplet in a perfect dielectric medium. In dielectric fluids, the dynamic current values are negligible [40,45,46]. In the absence of current flow and magnetic field, the charge movement is very slow. The characteristic time for the magnetic phenomena $t_m=\mu_M K l^2$ is several orders of magnitude smaller than the characteristic time for electric phenomena i.e. the electric relaxation time $t_e$ [43,44]. The value of $t_m$ in air and DI water are $3.77e^{-25}s$ and $1.72e^{-18}s$, respectively. The values of $t_m$ in air and DI water are much smaller as compared to the values of $t_e$. Thus, electrohydrodynamics of dielectric fluids can be regarded as a quasi-static model, which ignores the current flow and the induced magnetic effects [35,40,45,47]. Thus, the electrostatic phenomena can be described as

$$\nabla\times\vec{E}=0 \tag{16}$$

and

$$\nabla.\left(\varepsilon\vec{E}\right)=q \tag{17}$$

The electric field is calculated as the divergence of electric potential $V$

$$\vec{E}=-\nabla V \tag{18}$$

Thus, the electrostatic field can be expressed in terms of electric potential $V$

$$\nabla.(\varepsilon\nabla V)=-q \tag{19}$$

The transient charge density distribution inside the domain is obtained by solving the complete Nernst-Planck equation for charge transport [28]

$$\frac{\partial q}{\partial t}+\nabla.\mathbf{J}=0 \tag{20}$$

here, $\mathbf{J}=K\vec{E}+q\vec{u}-\psi\nabla q$ is the electric charge flux [27], $K$ is the electric conductivity, and $\psi$ is the ionic diffusivity. The inherent ion concentration in dielectric fluids (zero in air and infinitesimally small quantity in DI water) is very low. Due to the leaky dielectric nature of the droplet, the surface charges will instantaneously accumulate at the liquid-gas interface ($t_e<<t_h$). Thus, ionic diffusion in bulk is negligible and in general, ionic diffusion coefficients $\psi$ of dielectric fluids are very low [29,34]. Thus, the diffusion term is ignored. The permittivity and conductivity are considered as a harmonic function of phase fraction $\alpha$ as given in Eqs. (21) and (22)

$$\frac{1}{\varepsilon}=\frac{\alpha}{\varepsilon_1}+\frac{1-\alpha}{\varepsilon_2} \tag{21}$$

$$\frac{1}{K}=\frac{\alpha}{K_1}+\frac{1-\alpha}{K_2} \tag{22}$$

In the context of two-phase electrohydrodynamic flows, there are several approximated models reported in literature based on the conductivity of the working fluids [35,44,47–49]. A brief summary of the equations used to model the electrostatic phenomena in two-phase EHD flows are presented in Table 2. When both fluids are perfectly dielectric, there are no free charges. Thus, the Laplacian equation for electric potential is solved. There is no need to solve the charge transport equation, as the system is devoid of any free charges. The electrostatic force at the interface has only the normal stress (dielectrophoretic) component. When both the liquids are conducting liquids, Poisson equation for electric potential is solved. Due to the significant electrical conductivity of both the fluids, free charges will be instantaneously conducted due to electromigration. Thus, the charge transport equation is reduced to have only the electromigration term, as the temporal and the convective derivatives are very small. The electrostatic force will only have the normal stress component. When both the fluids are leaky dielectrics, Poisson equation for electric potential is solved. Even in the leaky dielectrics $t_e<<t_h$. Thus, the contribution of temporal and convective derivatives will be small. Therefore, the charge transport equation can be reduced only to the electromigration term. There will be accumulation of charges at the interface. Hence, the electrostatic force at the interface will have both the tangential and normal stress components. In the present work, a system of a leaky dielectric droplet in a perfect dielectric surrounding is considered. Thus, there will be free charges. Hence, we solve the Poisson equation for electric potential. $t_e<<t_h$ in the droplet and $t_e>>t_h$ in the surrounding medium. Thus, temporal derivative cannot be totally eliminated. Unlike a stationary, freely suspended droplet, present work considers a impacting droplet over a heated electrode surface. Thus, the interface undergoes significant deformation with respect to time and also there is a buoyancy induced flow. Thus, the convection component of charge transport equation cannot be ignored. Hence, the complete charge transport equation is considered in the present study (only the charge diffusion is neglected). Due to the accumulation of charges at the interface, both the normal and tangential stresses are considered. This approach has also been employed in previous studies reported in literature [29,30,32].

## 2.3. Governing parameters and variables

The driving parameters and results of this study are presented and analyzed using non-dimensional and normalized variables. In this problem configuration, the droplet impact dynamics is affected by inertial force, interfacial surface tension and electrostatic force. Effects of these factors are characterized by Weber number $We$ and electric capillary number $Ca_E$, that are defined as

$$We=\frac{\rho_1 {U_0}^2 D_0}{\sigma}\ \text{and}\ Ca_E=\frac{D_0\varepsilon_2|E_\infty|^2}{\sigma} \tag{23}$$

In the above equations, $E_\infty=\Delta V_0/L_H$. Furthermore, the thermal buoyancy force inside the flow domain is characterized by the Rayleigh number

$$Ra=\frac{g\xi_2\Delta\theta H^3}{\nu_2\alpha_{T2}} \tag{24}$$

**Table 2**
Summary of electrostatic equations used in two-phase EHD flows [35,44,47–49].

| | Perfect dielectric fluids | Conducting fluids | Leaky dielectric fluids | Leaky dielectric - Perfect dielectric fluids (Present work) |
|---|---|---|---|---|
| Electric potential | $\nabla^2(\varepsilon V) = 0$ | $\nabla^2(\varepsilon V) = -q$ | $\nabla^2(\varepsilon V) = -q$ | $\nabla^2(\varepsilon V) = -q$ |
| Charge conservation | Not applicable | $\nabla.\left(K\vec{E}\right) = 0$ | $\nabla.\left(K\vec{E}\right) = 0$ | $\frac{\partial q}{\partial t} + \nabla.\left(K\vec{E} + q\vec{u}\right) = 0$ |
| Electrostatic force | $\vec{F}_{es} = -\frac{1}{2}\vec{E}.\vec{E}\nabla\varepsilon$ | $\vec{F}_{es} = -\frac{1}{2}\vec{E}.\vec{E}\nabla\varepsilon$ | $\vec{F}_{es} = q\vec{E} - \frac{1}{2}\vec{E}.\vec{E}\nabla\varepsilon$ | $\vec{F}_{es} = q\vec{E} - \frac{1}{2}\vec{E}.\vec{E}\nabla\varepsilon$ |

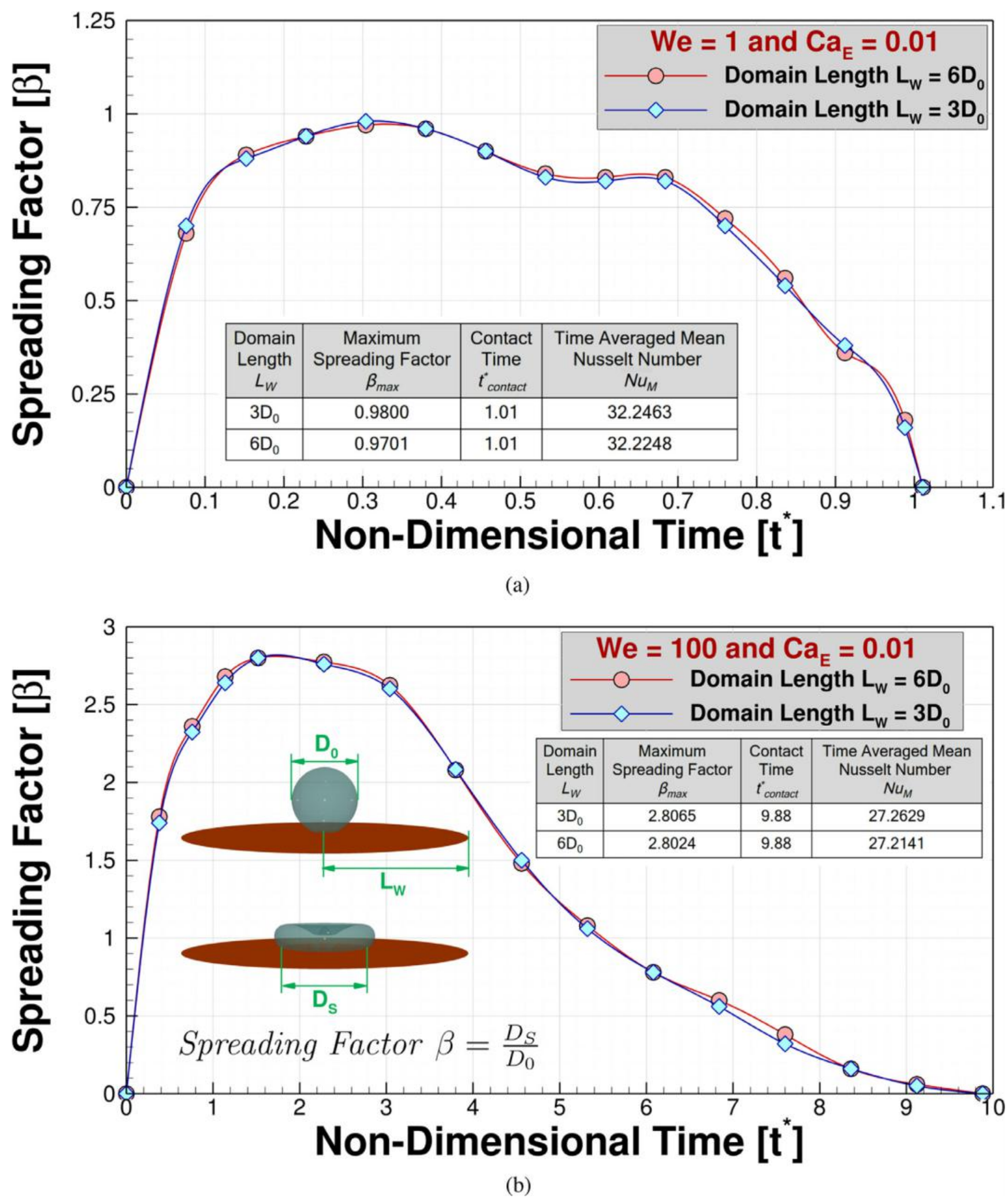


**Fig. 2.** Domain size independence analysis. Time evolution of spreading factor for (*a*) $Ca_E = 0.01$ and $We = 1$ and (*b*) $Ca_E = 0.01$ and $We = 100$. The inset table in the figure presents the maximum spreading factor, total contact time and time averaged mean Nusselt number.

where, $\xi$ is the thermal expansion coefficient, $\nu$ is the kinematic viscosity and $\alpha_T$ is the thermal diffusivity. The value of the Rayleigh number is considered as $Ra = 1 \times 10^3$ for all the simulations presented in this study. The parameter that represents the ratio of gravitational force to the capillary force is the Bond number. Bond number is expressed as

$$Bo = \frac{\Delta\rho g D_0^2}{\sigma} \tag{25}$$

For all the simulations carried out in this study, the Bond number is 0.034.

The thermophysical properties of the fluids are characterized by the Prandtl number $Pr = (\mu C_p)/k$. In this study, $Pr_1 = 6.31$ and $Pr_2 = 0.57$ with viscosity ratio $\mu_R = \mu_1/\mu_2 = 60.9$ and density ratio $\rho_R = \rho_1/\rho_2 = 773.6$. Furthermore, the dielectric permittivity ratio $\varepsilon_R = \varepsilon_1/\varepsilon_2 = 80.39$ and electrical conductivity ratio $K_R = K_1/K_2 = 4.58 \times 10^6$. The properties of the work-

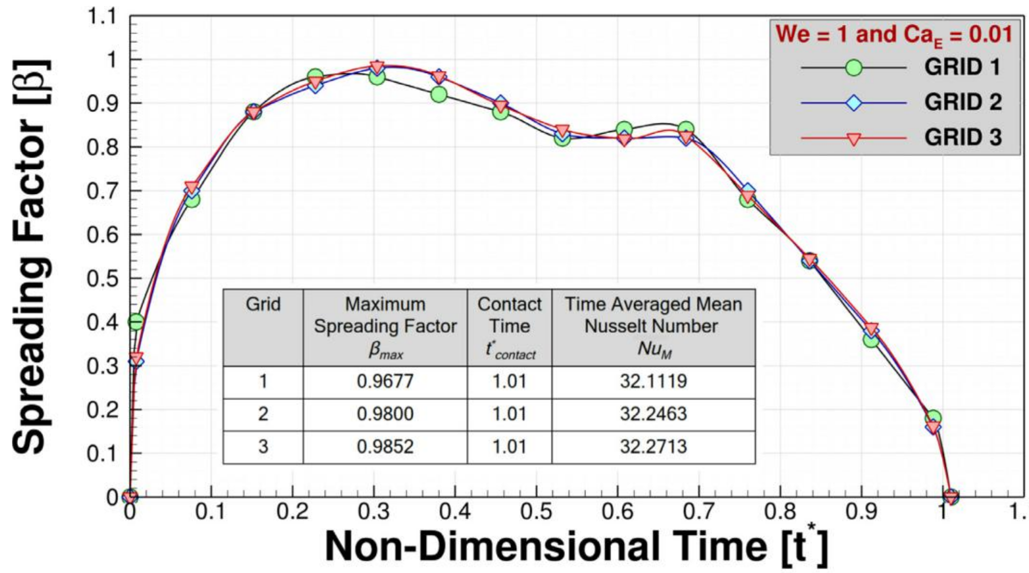


(a)

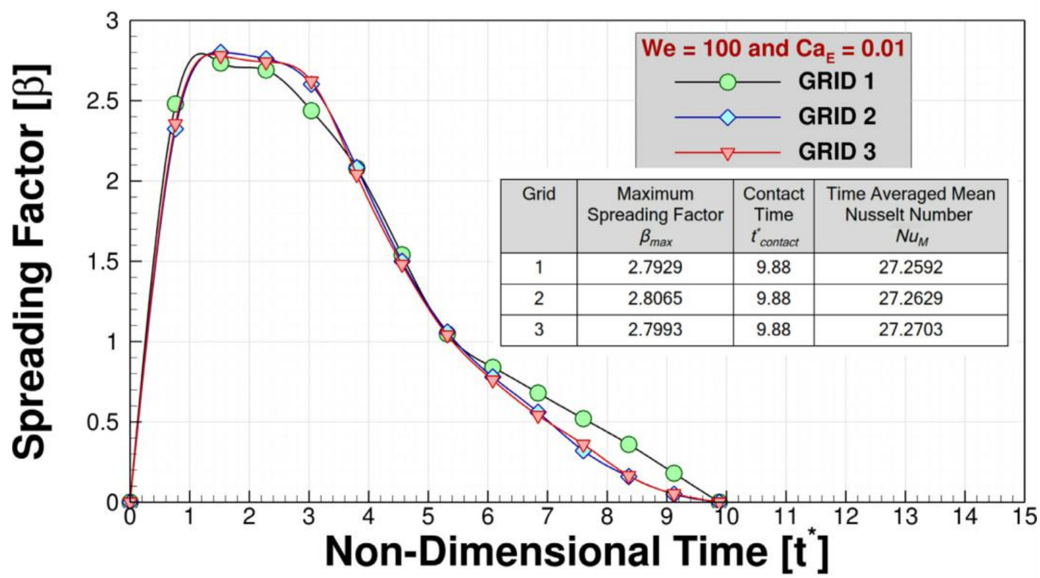


(b)

**Fig. 3.** Grid independence study. Time evolution of spreading factor for (*a*) $Ca_E = 0.01$ and $We = 1$ and (*b*) $Ca_E = 0.01$ and $We = 100$. The inset table in the figure presents the maximum spreading factor, total contact time and time averaged mean Nusselt number.

ing fluids are listed in Table 3. In addition, $We$ is varied in the range of $1 \leq We \leq 100$ such that the droplet remains in the bouncing regime and splashing does not occur. Hence, the axisymmetric assumption holds valid. The electric capillary number $Ca_E$ is varied in three levels 0, 0.01 and 0.1 where, $Ca_E = 0.1$ corresponds to a maximum electric potential of 10 $kV$ (approx). Since the electric field influences the gas-liquid surface tension [27], it would be more appropriate to use a model that calculates the dynamic contact angle as a function of the electric field for a charged droplet. Unfortunately, no such models are available in the literature. As a compromise, the present study utilizes a constant contact angle of 156° at the droplet three-phase contact line as recommended by Li et al. [50] for the considered range of parameters and operating conditions. Although this treatment is not ideal, it can predict the droplet impact behavior with acceptable accuracy, as showcased in the detailed validation study presented in Appendix A.

**Table 3**
Properties of working fluids.

| Thermophysical properties | Value |
|---|---|
| Density - Air [$kgm^{-3}$] | 1.29 |
| Density - DI water [$kgm^{-3}$] | 998 |
| Dynamic Viscosity - Air [$kgm^{-1}s^{-1}$] | $1.48 \times 10^{-5}$ |
| Dynamic Viscosity - DI water [$kgm^{-1}s^{-1}$] | $9.01 \times 10^{-4}$ |
| Thermal Conductivity - Air [$Wm^{-1}K^{-1}$] | 0.026 |
| Thermal Conductivity - DI water [$Wm^{-1}K^{-1}$] | 0.6 |
| Specific Heat Capacity - Air [$Jkg^{-1}K^{-1}$] | $1.01 \times 10^{03}$ |
| Specific Heat Capacity - DI water [$Jkg^{-1}K^{-1}$] | $4.20 \times 10^{03}$ |
| Surface Tension [$Nm^{-1}$] | $7.20 \times e^{-02}$ |
| **Dielectric Properties** | **Value** |
| Dielectric Permittivity - Air [$Fm^{-1}$] | $8.85 \times 10^{-12}$ |
| Dielectric Permittivity - DI water [$Fm^{-1}$] | $7.12 \times 10^{-10}$ |
| Electrical Conductivity - Air [$Sm^{-1}$] | $1.20 \times 10^{-12}$ |
| Electrical Conductivity - DI water [$Sm^{-1}$] | $5.50 \times 10^{-6}$ |

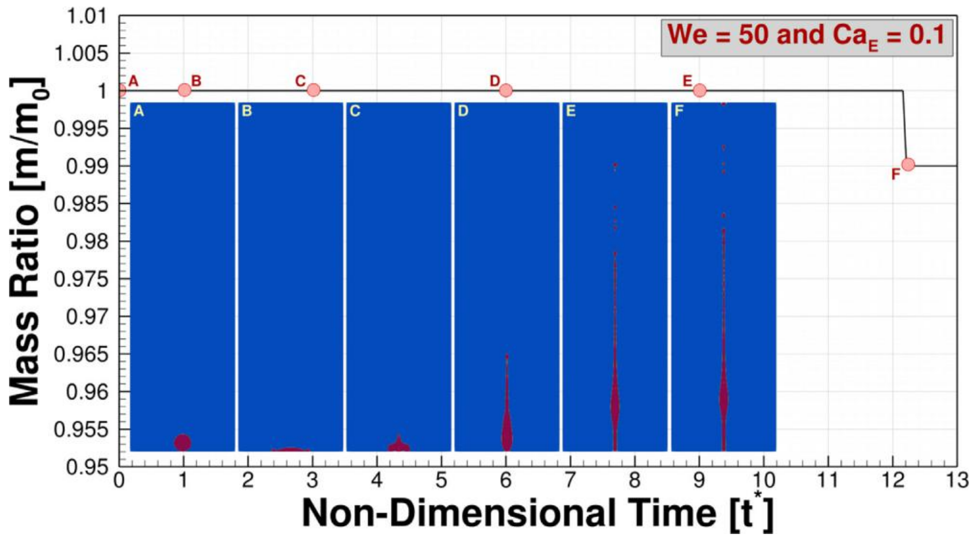


**Fig. 4.** Demonstration of mass conservation with time evolution of droplet mass ratio at $We = 50$ and $Ca_E = 0.1$. The inset images present the liquid fraction distribution at different instantaneous moments during the impact and bouncing process.

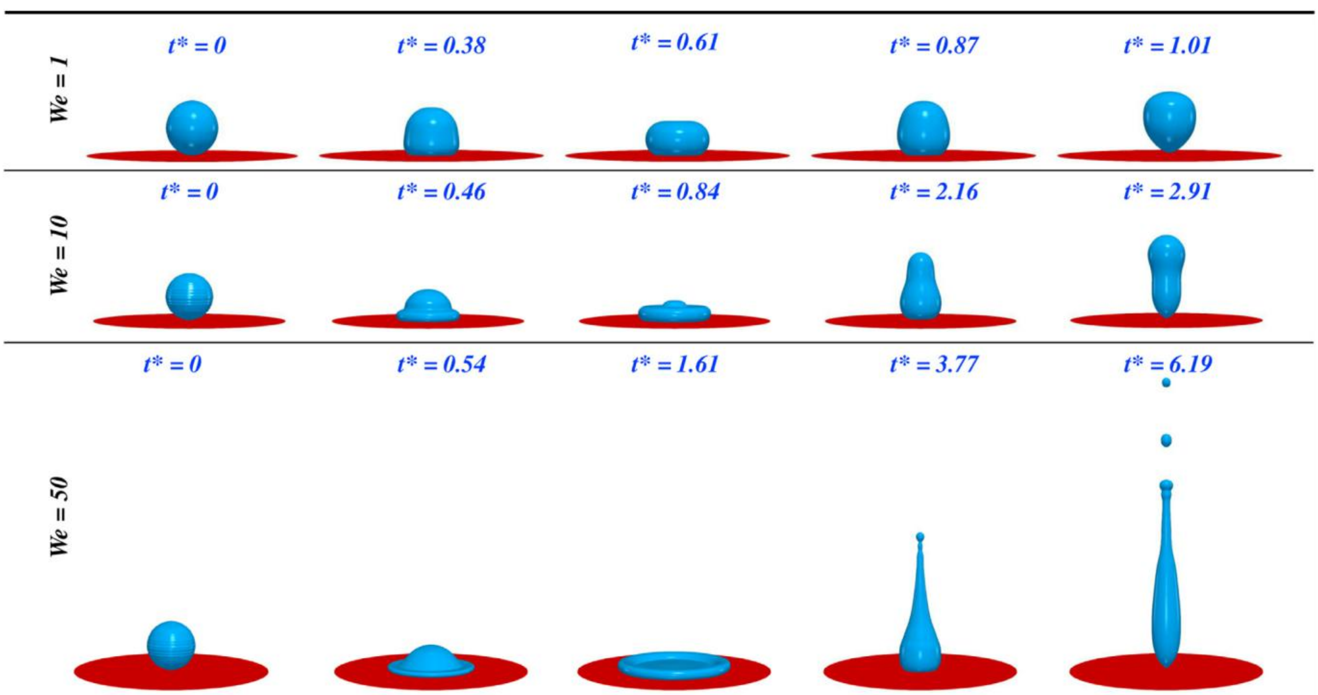


**Fig. 5.** Isocontours of $\alpha = 0.5$ at different time instances to demonstrate droplet behavior in different modes of bouncing in the absence of electric field ($Ca_E = 0$). First row: Quick bounce - M1, Second row: Bounce after deformation - M2 and Third row: Bounce with satellite droplets - M3..

## 3. Numerical methodology

The coupled set of governing equations for the two-phase ETHD flow based on a CLSVOF approach are implemented in the open-source finite-volume framework of OpenFOAM®. Using a collocated grid system, all the variables are stored at the center of control volumes. Standard second-order accurate finite-volume procedures available in OpenFOAM® are employed to discretize the governing equations [51]. A second-order accurate central differencing scheme is used to discretize the Laplacian terms and a third-order accurate cubic scheme is used to discretize the gradient terms. In general, convective terms are discretized using a third-order accurate QUICK scheme [52] except the convective term in the charge conservation equation, which is discretized using a second-order accurate total variation diminishing (TVD) Van Leer scheme [53]. The TVD scheme ensures an oscillation-free stable solution for the convection dominant charge conservation equation. Implicit Euler back ward method is employed to discretize all the time derivatives. A sequential, iterative solution procedure based on the PIMPLE algorithm is employed to solve the discretized equations [54]. The sparse matrices produced as a result of the discretization procedure are solved using a pre-conditioned bi-conjugate gradient

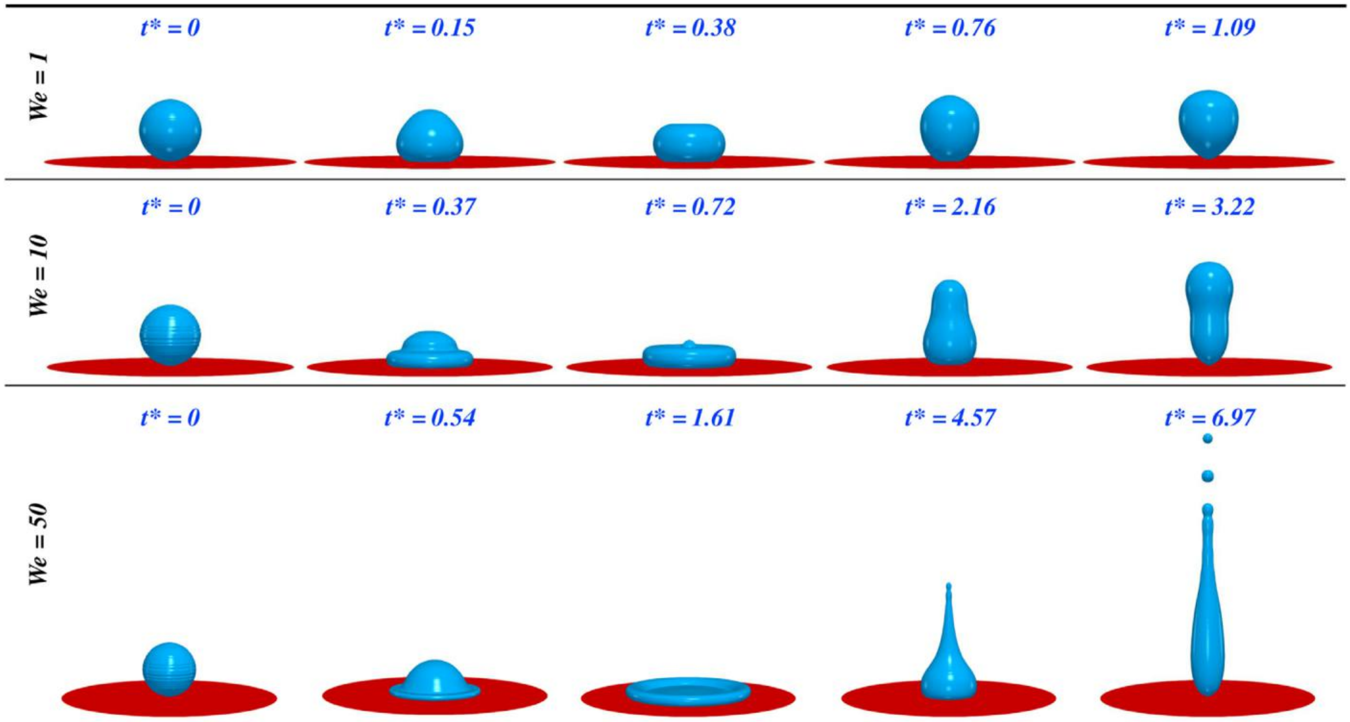


**Fig. 6.** Isocontours of $\alpha = 0.5$ at different time instances to demonstrate droplet behavior in different modes of bouncing in the presence of electric field ($Ca_E = 0.01$). First row: Quick bounce - M1, Second row: Bounce after deformation - M2 and Third row: Bounce with satellite droplets - M3..

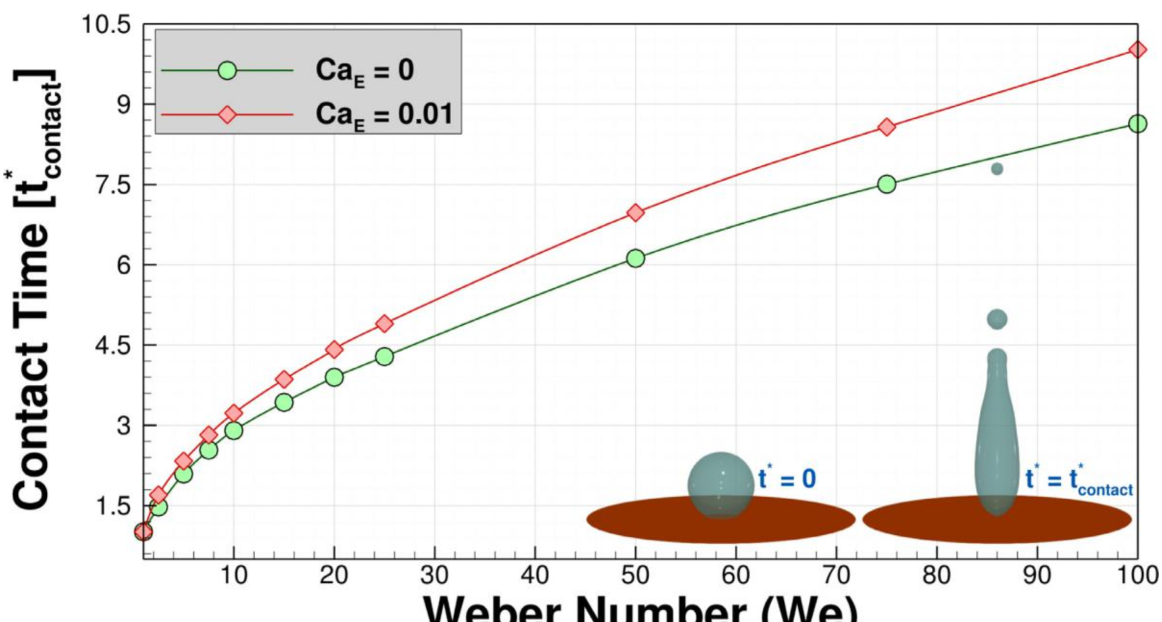


**Fig. 7.** Variation of total contact time of the droplet with the heated surface at $1 \le We \le 100$ and $Ca_E = 0$ and 0.01.

(PBiCG) method along with a diagonal incomplete-LU (DILU) pre-conditioner, for non-symmetric matrices. For symmetric matrices, geometric-algebraic multi-grid (GAMG) method coupled with a diagonal incomplete-Cholesky (DIC) pre-conditioner is utilized. The absolute tolerance for the sparse matrix solvers is set at $10^{-7}$.

## 4. Domain and grid independence analysis

The domain size and grid resolution used in this study are chosen based on a detailed domain and grid independence analysis. The domain height is set to $20 \times D_0$ to steer clear of the effect of the top boundary. The effect of domain width is presented in Fig. 2. Two domain widths $L_W = 3 \times D_0$ and $6 \times D_0$ have been considered for the domain independence study. Likewise, grid independence study results are presented in Fig. 3. Three different grids with 200,000, 400,000 and 800,000 cells have been considered. The domain and grid independence have been checked with respect to various parameters such as spreading factor $\beta$, maximum spreading factor $\beta_{\max}$, total non-dimensional contact time $t^*_{contact}$

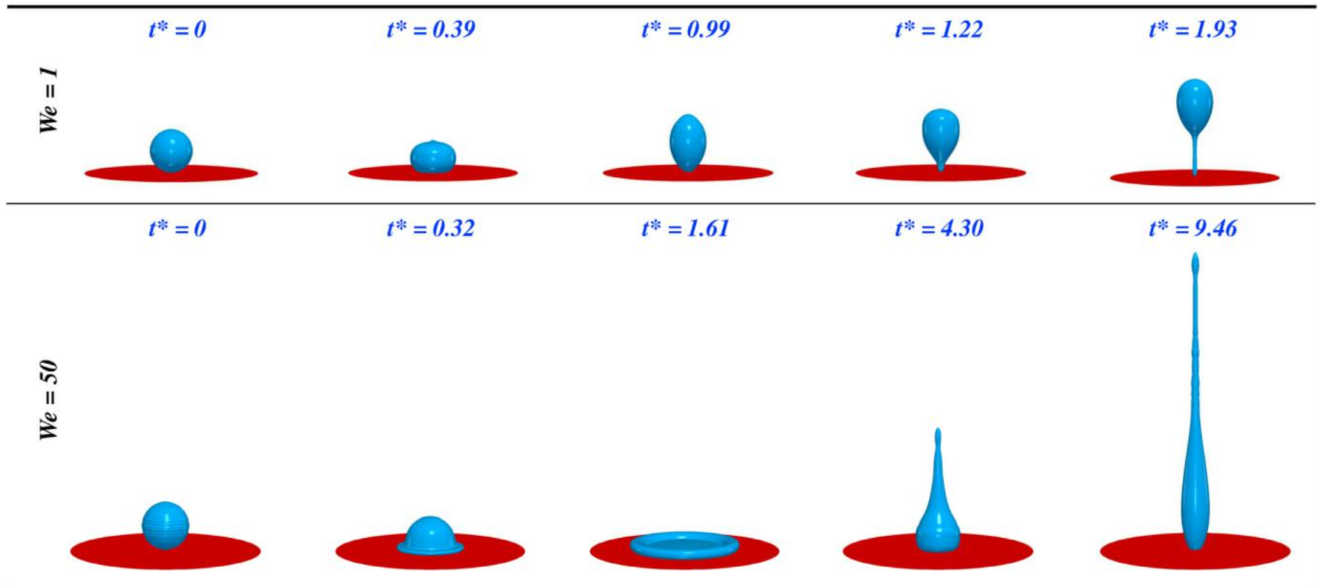


**Fig. 8.** Isocontours of $\alpha = 0.5$ at different time instances to demonstrate droplet behavior in different modes of bouncing in the presence of electric field ($Ca_E = 0.1$). First row: Bounce with tail in the bottom tip - M4 and Second row: Upward stretching - M5..

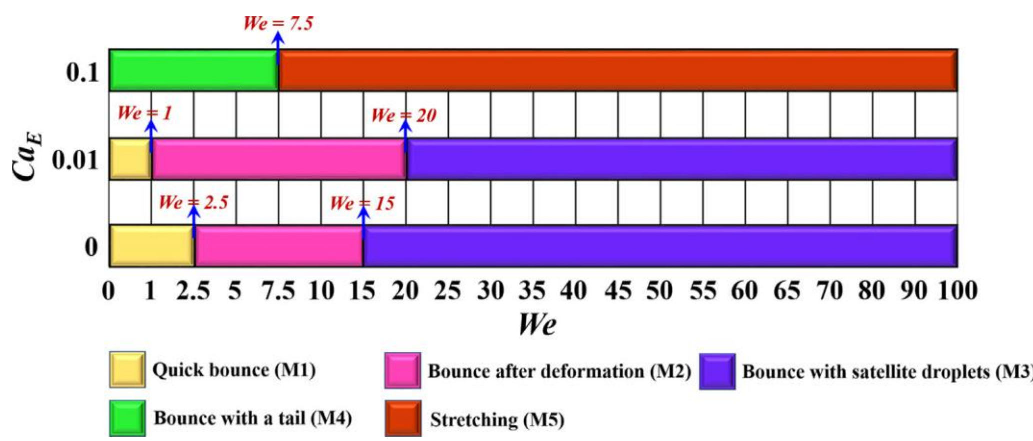


**Fig. 9.** Droplet bouncing modes observed at $1 \leq We \leq 100$ and $0 \leq Ca_E \leq 0.1$.

and time averaged mean Nusselt number $Nu_M$. Spreading factor $\beta$ is defined as follows:

$$\beta = \frac{\text{Width of the droplet in contact with the solid surface}}{\text{Initial diameter of the droplet}} = \frac{D_S}{D_0} \tag{26}$$

where, $\beta_{\max}$ is the maximum value of $\beta$ observed at the stage when the droplet is at its maximum spreading point and $t^*_{contact}$ is the total non-dimensional time duration for which the droplet is in contact with the solid surface, before it bounces off. The non-dimensional time $t^*$ is given by

$$t^* = \frac{U_0 t}{D_0} \tag{27}$$

Local Nusselt number is calculated along the heated bottom surface as

$$Nu_L = \frac{\frac{\partial(\theta_w - \theta)}{\partial y} L_W}{\theta_W - \theta_\infty} \tag{28}$$

Mean Nusselt number is calculated by the average of $Nu_L$ along the length $L_W$. Time averaged mean Nusselt number $Nu_M$ is the mean Nusselt number over the hot surface, averaged over a period of time equal to $t^*_{contact}$. Based on the results presented in Figs. 2 and 3, GRID 2 with 400,000 cells and $L_W = 3D_0$ have been chosen for this study. In addition to the grid and domain independence studies, the mass conservation characteristics of the numerical model are also presented in Fig. 4. The mass ratio is the ratio of the droplet mass ($m$) at a specific time moment to its initial mass ($m_0$). Different stages of droplet deformation namely impact, spreading, retracting, stretching and breaking up into satellite droplets, are marked as points A, B, C, D, and (E & F), respectively. It is observed that the mass ratio remains perfectly as 1, until the first satellite droplet leaves out of the domain at point F. Thus, it is evident that the numerical model used in this study guarantees mass conservation until or unless the droplet escapes from the domain. An adaptive time-stepping method has been used such that the total and interface Courant numbers are always less than or equal to 0.25.

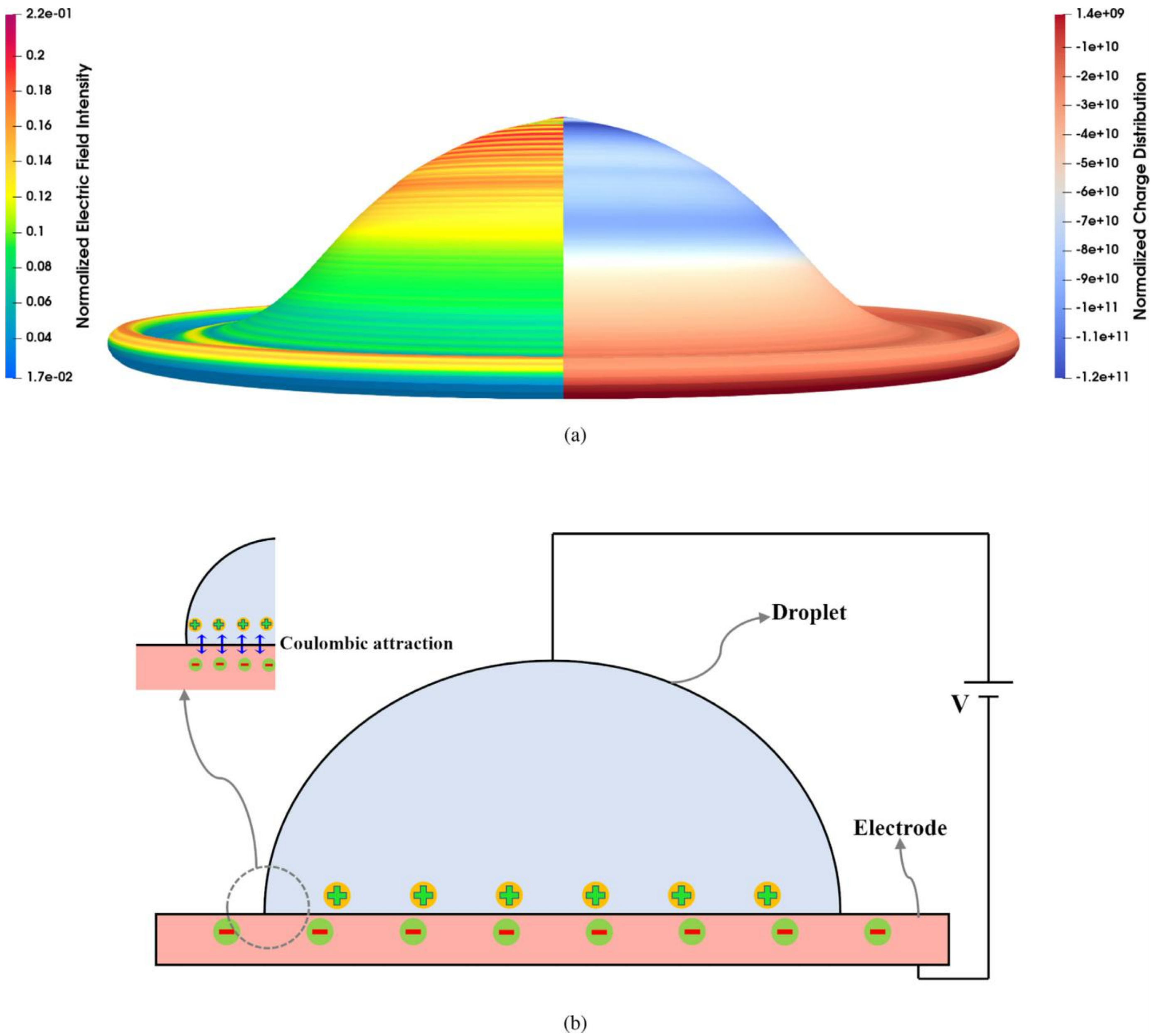


**Fig. 10.** ($a$) Contours of normalized electric field (left) and normalized charge distribution in the droplet at instantaneous time step at $We = 50$ and $Ca_E = 0.1$. ($b$) Schematic diagram of the charge distribution and Coulombic attraction near the solid-liquid contact line.

## 5. Results and discussion

This section presents a detailed analysis and discussion of the results obtained in this numerical study. Firstly, the dynamics and bouncing modes of the droplet at different Weber number ($We$) and electric Capillary number ($Ca_E$) are discussed in Section 5.1. Then, in Section 5.2, the mechanism of droplet stretching observed in the presence of an electric field is explained. Finally, the heat transfer characteristics during the droplet stretching due to the electric field is highlighted in Section 5.3.

### 5.1. Droplet dynamics and modes

Once the droplet impacts a flat solid surface, the droplet begins to spread due to the kinetic energy. The extent of spreading is dependent on the initial impact velocity determined by the Weber number $We$. On reaching its maximum spreading diameter, the surface energy due to the surface tension causes the droplet to retract. This retraction continues further to make the droplet tip/apex stretch upward. Finally, the stretched droplet may bounce off the surface as a whole droplet or bounce along with some small satellite droplets, that break up from the original droplet. Different modes of bouncing of droplets in the parameter space considered in this study are presented in Figs. 5, 6 and 8. The droplet visualizations are isocontours drawn at $\alpha = 0.5$. In the absence of electric field i.e., $Ca_E = 0$, depending on the $We$, the droplet exhibits three bouncing modes namely, M1- quick bounce, M2 - bounce after deformation and M3 - bounce with satellite droplets. The three modes of droplet bouncing seen in the absence of electric field ($Ca_E = 0$) are presented in Fig. 5. In M1, the droplet undergoes only a slight deformation on impact. In other words, the droplet spreading over the surface is minimal. Then, the droplet retracts and

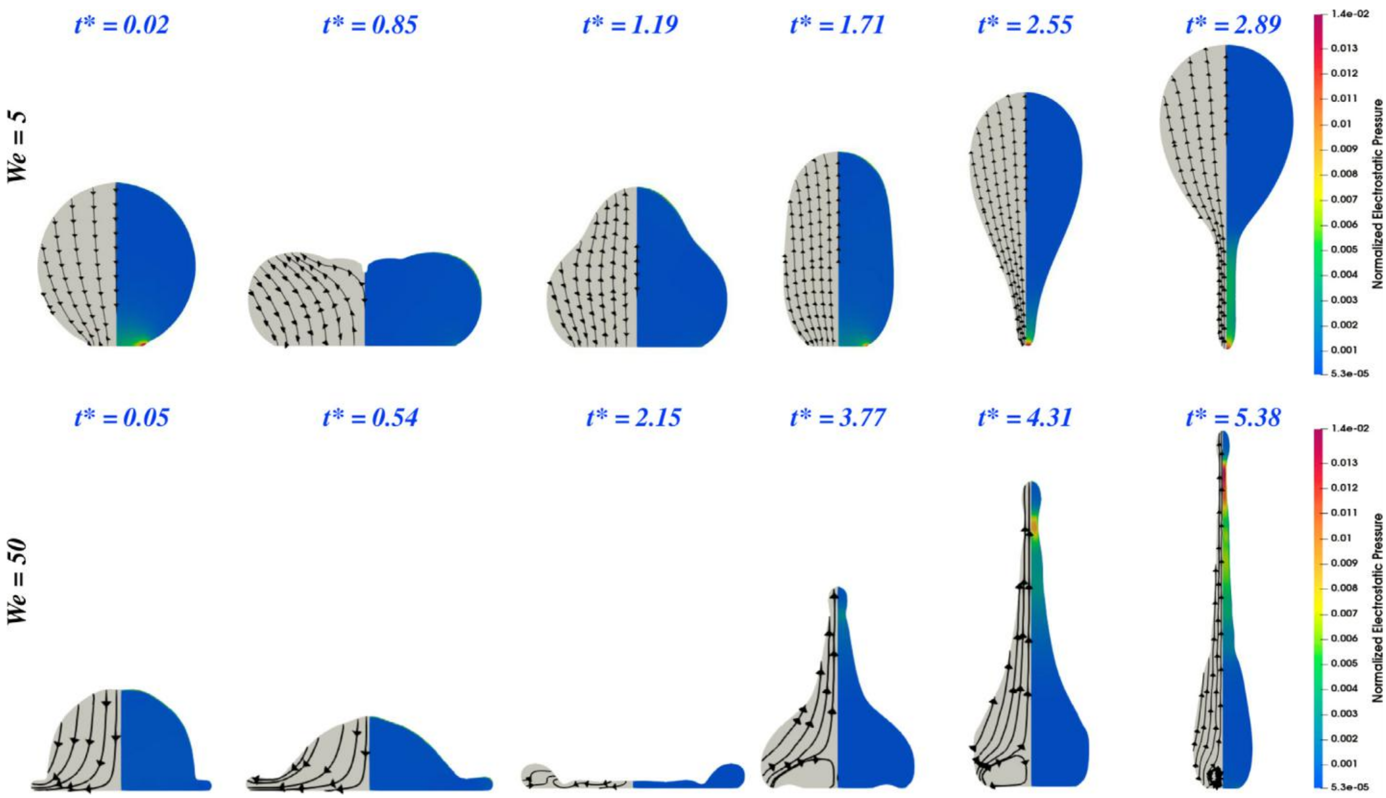


**Fig. 11.** Instantaneous distribution of normalized electrostatic pressure and streamline contours at $Ca_E = 0.1$ and $We = 5$ and 50. (Note : The droplet size is not to scale. All images are zoomed for visibility.).

bounces off the surface, almost retaining its original shape. In M2, the droplet impacts the surface and undergoes significant deformation, spreading more or less to a disc shape. Then, the droplet retracts and bounces from the solid surface. The droplet is well deformed to a calabash shape, while bouncing. Finally, the third mode M3 is characterized by impact, significant spreading, retraction, breakup of small satellite droplets and bouncing along with satellite droplets. The main droplet is deformed to the shape of a snow bowling pin, at the moment of bouncing. At $1 \le We \le 2.5$, mode M1 is observed, mode M2 is seen for $2.5 < We \le 15$ and when $15 < We \le 100$ mode M3 is noted. The maximum value of $We$ is limited to 100, to restrict only to the bouncing regime. Beyond $We = 100$, the droplet exhibits splashing at the end of the spreading stage. To accurately resolve the splashing of droplets, a 3D study is required. Thus, the present study limits the maximum value of $We$ to 100.

For electric capillary number $Ca_E = 0.01$, the same three modes M1, M2, and M3 are exhibited (refer Fig. 6), while the transitions are slightly shifted with respect to $We$. Mode M1 is observed only up to $We = 1$. For $1 < We \le 20$, mode M2 is exhibited and mode M3 is seen for $We > 20$. This indicates that the electrostatic force promotes deformation of the droplet, as already inferred by Ryu et al. [27]. Thus, the quick bounce mode M1 is seen only for a short range of $We$. It is also to be noted that the total contact time $t^*_{contact}$ of the droplet with the bottom surface has increased. For instance, at $We = 10$ the total non-dimensional contact time is 2.91 for $Ca_E = 0$. Whereas for $Ca_E = 0.01$, the total contact time at $We = 10$ is 3.22. The comparison of total contact time at $Ca_E = 0$ and 0.01 is shown in Fig. 7. The $t^*_{contact}$ is higher for $Ca_E = 0.01$ and also, the difference is more pronounced at higher Weber numbers. A maximum of 13% increase in total contact time is observed at $We = 100$. Thus, it can be inferred that the electric field increases the total contact time at $Ca_E = 0.01$, as compared with $Ca_E = 0$.

The dynamic droplet modes for $Ca_E = 0.1$ are presented in Fig. 8. Different from aforementioned results for $Ca_E = 0$ and 0.01, two new modes are observed in this case, namely M4 - Bounce with a tail and M5- Stretching. For the case of $Ca_E = 0.1$ and $We = 1$ presented in the first row of Fig. 8, the droplet impacts the bottom surface, undergoes a slight deformation, retracts and then begins to bounce. But while bouncing, a small cross section of the droplet continues to be attached to the bottom wall. This elongates like a tail, as the droplet moves further upward. This elongated tail will eventually break into small secondary droplets. The mode M4 is observed at $1 \le We \le 7.5$. For $We > 7.5$, an upward stretching of the droplet (M5) is observed. As shown in the second row of Fig. 8, at $Ca_E = 0.1$ and $We = 50$, the droplet impacts the surface, deforms significantly to a disc shape, retracts and stretches vertically to form a thin, tall tip. This stretching continues until the top tip disintegrates into small satellite droplets. Following the stretching of the top end, the bottom end of the droplet also undergoes thinning and stretching (refer to inset image F of Fig. 4). The stretched droplet will eventually disintegrate into smaller secondary droplets. Thus, in the presence of stronger electric field ($Ca_E = 0.1$), two new modes of droplet dynamics are observed. For the case of $Ca_E = 0.1$, a precise $t^*_{contact}$ cannot be defined because the bottom tip of the droplet remains attached to the bottom surface for a very long time, before the top end disintegrates into satellite droplets and escapes out of the computational domain. The overall mapping of the different droplet dynamic modes seen over the range of $Ca_E$ and $We$ considered in this study, is presented in Fig. 9.

### 5.2. Mechanism of stretching in the presence of electric field

In Fig. 10a, the normalized electric field intensity ($E^* = E/E_\infty$) and normalized charge distribution in the droplet are presented at $t^* = 0.45$, $Ca_E = 0.1$ and $We = 50$, for better understanding of two

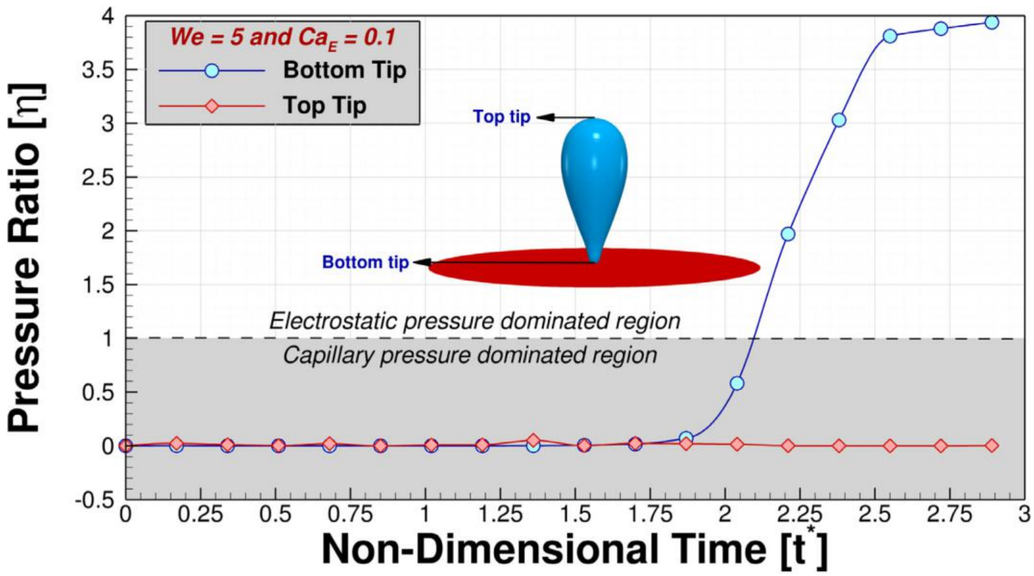


(a)

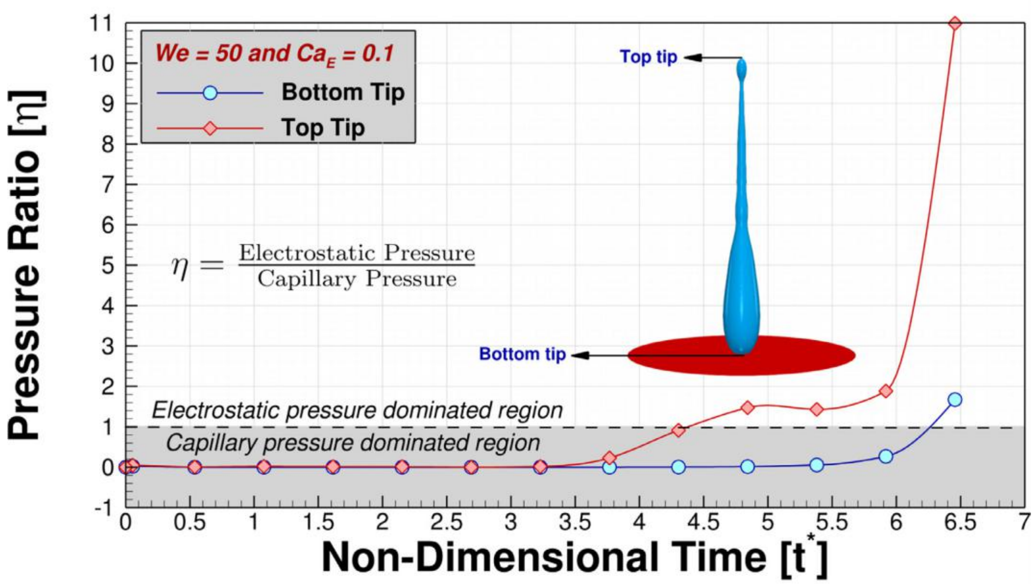


(b)

**Fig. 12.** Time evolution of pressure ratio ($\eta$) on the top and bottom tips of the droplet for ($a$) $We = 5$ and ($b$) $We = 50$, in the presence of electric field $Ca_E = 0.1$.

new modes M4 and M5. The normalized charge distribution is defined as

$$q^* = \frac{\frac{4}{3}\pi\left(\frac{D_0}{2}\right)^3 q}{e_0} \tag{29}$$

where, $e_0$ is the basic electric charge ($1.6 \times 10^{-19}C$). On the left side of Fig. 10a, the electric field distribution is stronger at locations with a high radius of curvature. This indicates that the local electric field distribution is a strong function of the local radius of curvature. Likewise on the right hand side of Fig. 10a, it is observed that the bottom edge of the droplet has a strong positive charge distribution. The top electrode, connected to the high voltage power supply, will have strong positive charge, while the bottom surface which is grounded will have a negative charge distribution. Due to the electric field, the droplet will also get charged. As a result, the bottom edge of the droplet accumulates positive charges. This phenomenon is presented in the schematic form in Fig. 10b. The liquid-solid contact line between the droplet and the bottom surface will experience a Coulombic attraction due to the accumulation of opposite charges in the bottom end of droplet and the bottom surface (grounded electrode). This Coulombic attraction between the bottom surface of the droplet and the grounded bottom electrode explains the longer contact time seen in the presence of the electric field.

In Fig. 11, the streamline contours and normalized electrostatic pressure distribution within the droplet is presented for $We = 5, 50$ at $Ca_E = 0.1$. The streamlines are pointing downwards during impact and spreading stages. The streamlines begin to point vertically upward during the retraction and stretching stages. The electrostatic pressure is defined as

$$p_e = \frac{1}{2}\varepsilon_2|E|^2 \tag{30}$$

The electrostatic pressure is normalized by the hydrostatic pressure. As already explained using Fig. 10a, the local electric field

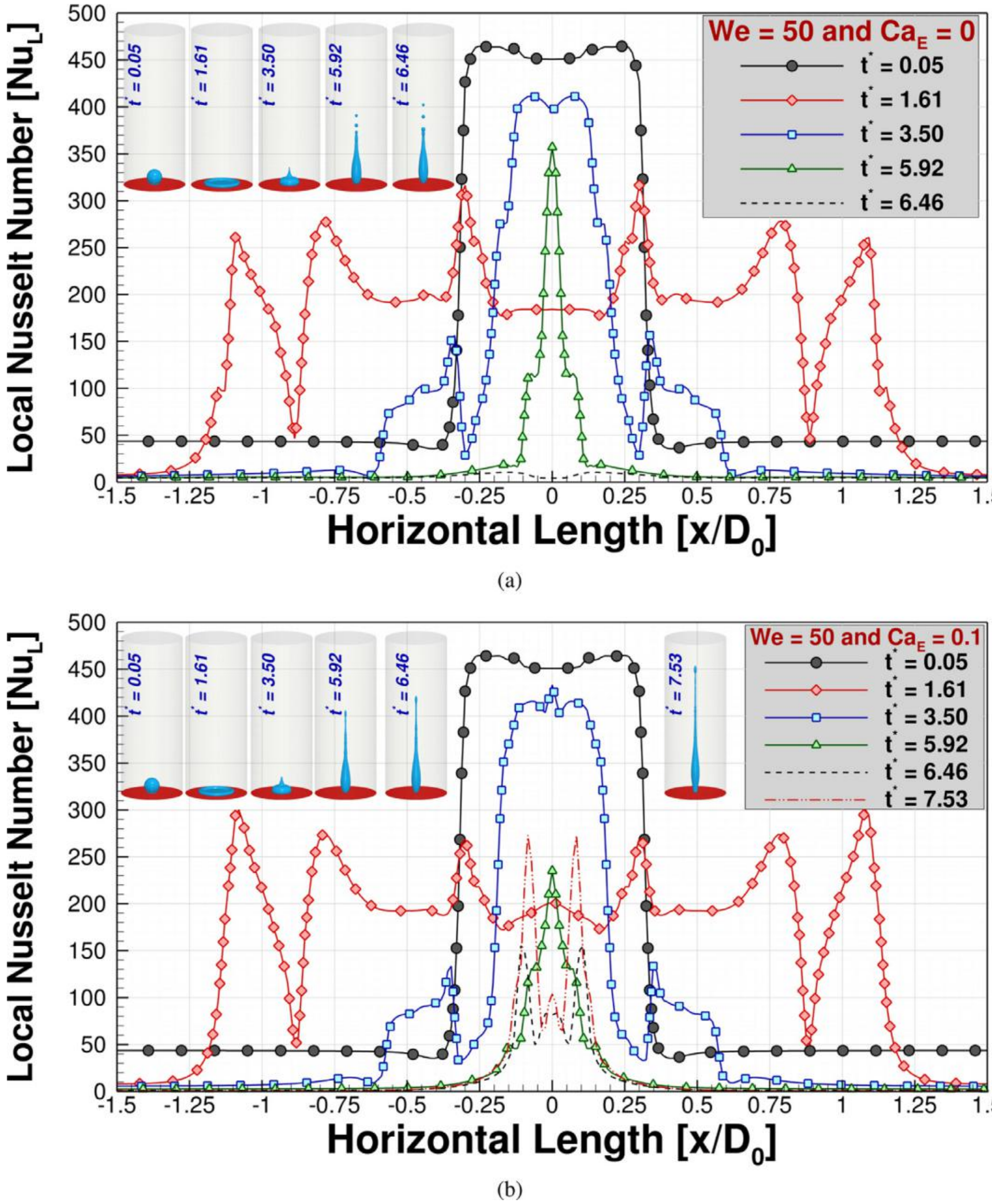


**Fig. 13.** Local Nusselt number distribution along the heated surface at $We = 50$. (*a*) $Ca_E = 0$ and (*b*) $Ca_E = 0.1$. The inset images show the droplet shape at different instantaneous moments.

distribution strongly influences the local curvature of the droplet. As a result, the local electrostatic pressure distribution within the droplet is strong over the region with sharp curvature. As shown in Fig. 11, for the case of $We = 5$ the shape evolution of the droplet favors the stronger electrostatic pressure distribution near the bottom tip of the droplet. Whereas, the shape evolution of the droplet at $We = 50$ favors the stronger electrostatic pressure distribution close to the top tip of the droplet. The stronger electrostatic pressure near the bottom end and the Coulombic attraction with the bottom electrode facilitates the formation of a bottom tail attached to the bottom surface, when $We = 5$. Similarly, the stronger electrostatic pressure distribution near the top tip of the droplet promotes upward stretching of the droplet, when $We = 50$. Thus, the electrostatic pressure distribution near the bottom or top end of the droplet and the Coulombic attraction near the solid-liquid contact line decide the formation tail or upward stretching.

The pressure ratio $\eta$ can further explain the mechanism of modes M4 and M5. The pressure ratio $\eta$ is defined as the ratio of electrostatic pressure to the capillary pressure $p_\sigma = 2\sigma/\kappa_a$. Here, $\sigma$ is the surface tension and $\kappa_a$ is the droplet's local curvature near the top/bottom apex. The capillary pressure causes the droplet to retract and retain its spherical shape. In other words, capillary pressure restricts the stretching. In contrast, the electrostatic pressure promotes the vertical stretching of the droplet. For $We = 5$ (see Fig. 12a), the initial stages of the droplet deformation at both the ends are dominated by the capillary pressure. At $t^*$ close to 1.85, the electrostatic pressure near the bottom tip begins to increase and at $t^* = 2.09$, the value of $\eta$ becomes greater than 1. This causes the bottom end of the droplet to stretch like a tail in the trailing end of the droplet. As shown in Fig. 12b, the value of $\eta$ becomes higher than 1 for the top tip at $t^*$ close to 4.35, in the case of $We = 50$. This explains the upward stretching of the droplet. Furthermore, at $t^* = 6.27$, the value of $\eta$ at the bottom

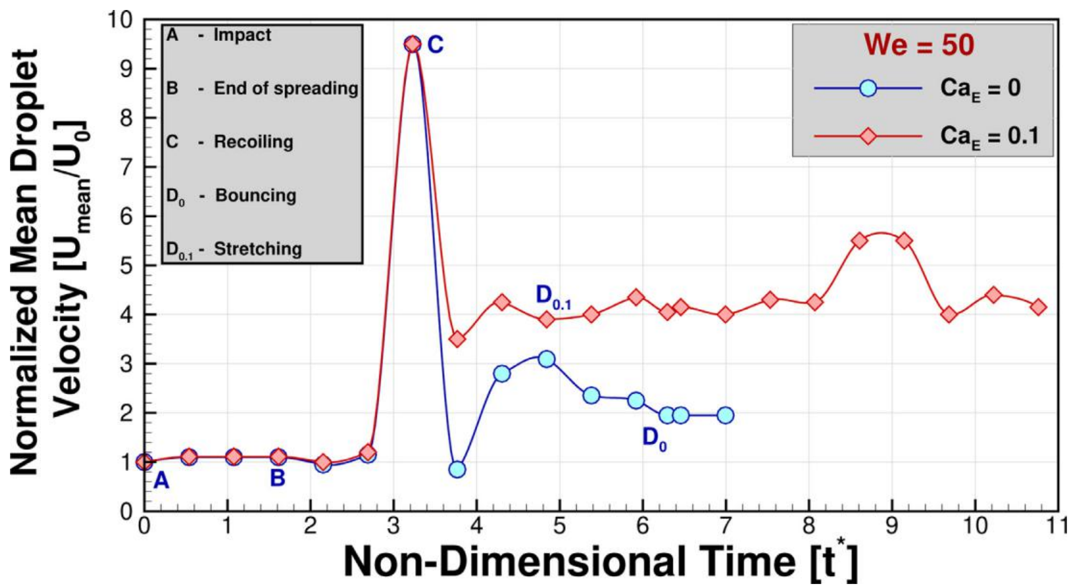


**Fig. 14.** Normalized mean velocity inside the droplet at $We = 50$ for $Ca_E = 0$ and 0.1.

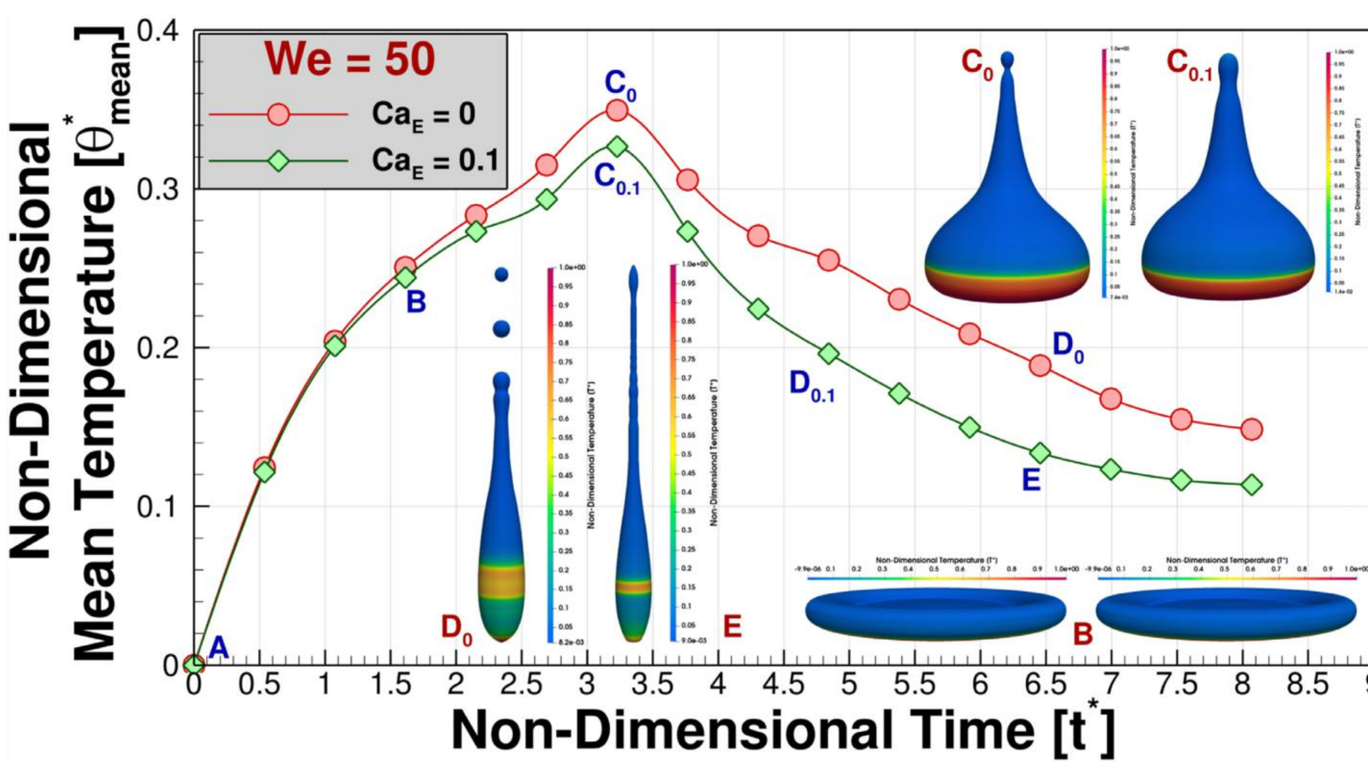


**Fig. 15.** Normalized mean temperature inside the droplet at $We = 50$ for $Ca_E = 0$ and 0.1. The inset images present the zoomed views of non-dimensional temperature distribution in the droplet at three different instantaneous moments.

end also becomes greater than 1. This can be related to the stretching of the bottom end of the droplet, as seen in the inset image F presented in Fig. 4. Thus, it can be inferred that the local curvature of the droplet and the related electric field distribution determine the occurrence of modes M4 and M5.

### 5.3. Heat transfer characteristics during droplet stretching

Finally, the heat transfer characteristics observed during the droplet stretching (M5) are discussed in this sub-section. The local Nusselt number $Nu_L$ distribution over the heated bottom surface for $We = 50$ at $Ca_E = 0$ and 0.1 are presented in Fig. 13a and b, respectively. Immediately after the impact, at $t^* = 0.05$, very high values of $Nu_L$ are observed in the droplet impact region at the heated bottom surface. At this point, the heat transfer characteristics are identical for both $Ca_E = 0$ and 0.1. With further progress in time, the droplet enters into the spreading stage. At $t^* = 1.61$, both the cases exhibit a more or less identical heat transfer characteristics, in the spreading stage. We can observe that the $Nu_L$ distribution is also a function of local liquid layer thickness. This is very evident in the $Nu_L$ distribution at $t^* = 1.61$. At $t^* = 1.61$, the droplet is almost stretched to its maximum extent like a disc. However, the disc is not smooth but, has ups and downs. The Local Nusselt number distribution shows sudden spikes where the liquid layer is thick and exhibits sharp falls where the liquid layer is thin. At $t^* = 3.50$, the droplet begins to recoil. The local Nusselt number distribution is also identical except for some minor differences. At $t^* = 5.92$, the droplet commences to bounce off from the bottom heated surface for $Ca_E = 0$. This is characterized by a sharp spike near the midpoint of the bottom surface. Whereas for $Ca_E = 0.1$, the droplet still remains attached to the surface, which can be related to the wider $Nu_L$ profile near the midpoint of the heated bottom surface. At $t^* = 6.46$, the droplet has completely bounced off from the surface for $Ca_E = 0$, which causes the $Nu_L$ to fall to very low values. Unlike the case without the electric field, the droplet does not bounce off the surface for $Ca_E = 0.1$. Instead, it remains attached to the surface and also stretches vertically upward. This can be correlated with the increase in $Nu_L$ distribution at $t^* = 6.46$ and 7.53. The upward stretching of the droplet makes it come in contact with the cooler region of the domain and facilitates the heat removal from the droplet. The variation in normalized mean velocity of the droplet is plotted in Fig. 14. The normalized mean velocity is the same until the recoiling stage. Once the droplet reaches the recoiling stage, the curves of $Ca_E = 0$ and 0.1 begin to deviate. The mean velocity of the droplet is higher for the case with electric field $Ca_E = 0.1$. This also explains the higher $Nu_L$ distributions in the stretching stage. Likewise, the non-dimensional mean droplet temperature is plotted in Fig. 15. The mean droplet temperature is more or less the same for both cases until the recoiling stage. Once the droplet enters the recoiling stage, the mean droplet temperature of the case with the electric field ($Ca_E = 0.1$) becomes lower than that of $Ca_E = 0$. This is due to the stronger velocity distribution caused by the electric field and elongated shape of the droplet, which helps it dissipate heat easily to the cooler top regions of the domain. Overall, the presence of an electric field increases the heat transfer by increasing the contact time, increasing the mean velocity in the droplet, and by better heat dissipation to the surrounding fluid.

## 6. Concluding remarks

This study numerically investigates the bouncing dynamics and heat transfer of a dielectric droplet over a heated solid surface in the presence of a vertical electric field. The electric field has a notable influence on the bouncing dynamics of the droplet. All the bouncing modes observed in the range of $We$ and $Ca_E$ considered in this study, has been mapped. Two new modes, M4 and M5, were identified at $Ca_E = 0.1$. In M4, the droplet bounces off with a tail that is attached to the heated bottom surface. M5 is characterized by stretching and thinning of the droplet. The electric field resulted in longer total contact times of the droplet due to the Coulombic attraction at the solid-liquid contact line. The local electric field distribution is observed to be strongly dependent on the local curvature of the droplet. The droplet stretching direction is decided by the instantaneous droplet curvature and electrostatic pressure distribution within the droplet. At $Ca_E = 0.1$, at lower Weber numbers mode M4 is observed, whereas higher values of $We$, favor the occurrence of M5. The stretching of the droplet in mode M5 influences the heat transfer significantly. The stretching droplet increases the heat transfer by longer contact time, enhanced fluid circulation within the droplet and better heat dissipation to the surrounding fluid.

## Declaration of Competing Interest

The authors declare that they have no known competing financial interests or personal relationships that could have appeared to influence the work reported in this paper.

## CRediT authorship contribution statement

**R. Deepak Selvakumar:** Conceptualization, Methodology, Data curation, Writing – original draft. **Hyoungsoon Lee:** Conceptualization, Supervision, Writing – review & editing.

## Acknowledgments

This research was supported by the Samsung Research Funding & Incubation Center of Samsung Electronics under project number SRFCTA1903, and the Korea Institute of Energy Technology Evaluation and Planning(KETEP) and the Ministry of Trade, Industry & Energy(MOTIE) of the Republic of Korea (No. 20214000000280).

## Appendix A. Code validation

This section presents a detailed validation of the numerical solver utilized in this study, which is developed in the open-source finite-volume framework of OpenFOAM®. Results obtained using the present solver are compared with standard experimental, numerical and analytical results of the physics involved in the context

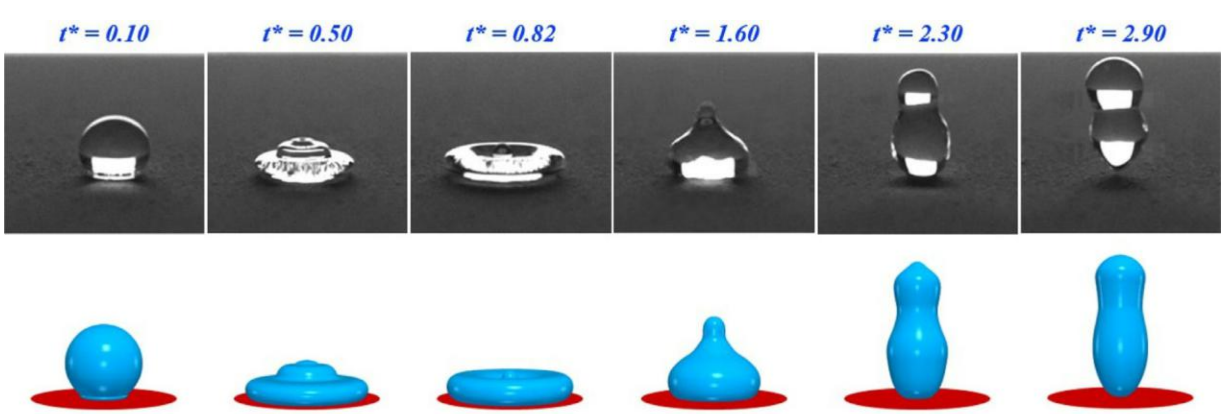


**Fig. A1.** Case 1: Qualitative comparison of droplet impact and deformation sequence at $U_0 = 0.64\,\mathrm{ms}^{-1}$ and $D_0 = 2.14\,\mathrm{mm}$. The first row corresponds to experimental results of Li et al. [50]. Second row shows isocontours of $\alpha = 0.5$ from present numerical simulations..

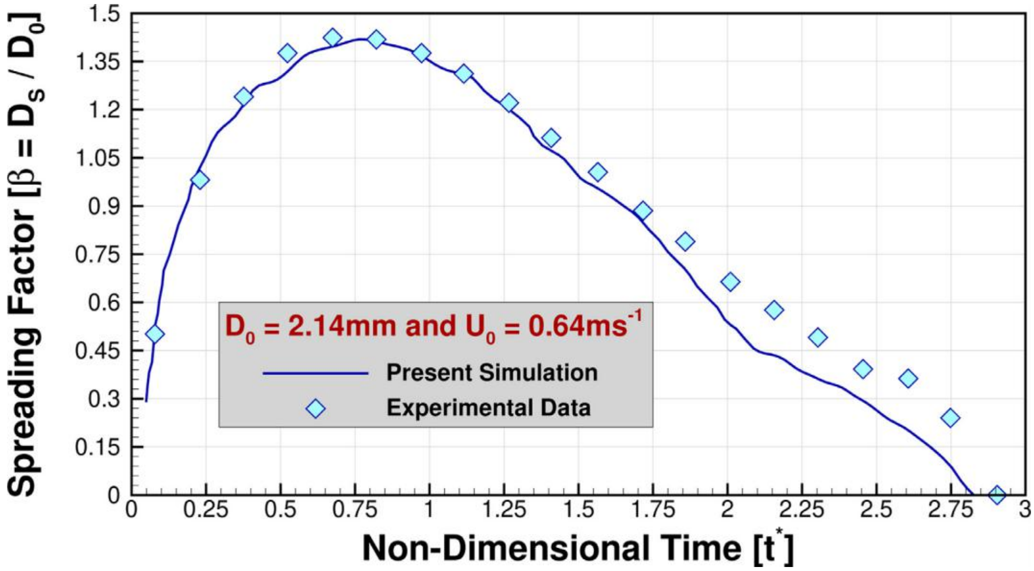


**Fig. A2.** Case 1: Time evolution of spreading factor for droplet impact over a solid surface at $U_0 = 0.64\,\mathrm{ms}^{-1}$ and $D_0 = 2.14\,\mathrm{mm}$. The symbols correspond to the experimental results of Li et al. [50].

of present study. To be specific, the numerical framework is tested with respect to following four benchmark cases:

- **Case 1:** Droplet impact over an isothermal solid surface [50].
- **Case 2:** Droplet impact over a heated solid surface [55,56].
- **Case 3:** Deformation of a freely suspended dielectric droplet in an external electric field [44,57].
- **Case 4:** Impact and bouncing of a droplet over an isothermal hydrophobic surface in an external electric field [32].

### *A1. Case 1: Droplet impact over an isothermal solid surface*

The numerical framework utilized in this study is first compared with the case of water droplet impact over a smooth solid hydrophobic surface. The numerical setup is exactly same as the case demonstrated in Figs. 3 and 4 of Ref [50]. In Fig. A.16, a qualitative comparison of numerical results with the experimental results of the droplet shape at different time instances during impact, spreading, recoiling and bouncing stages is presented by means of droplet visualizations using isocontours ($\alpha = 0.5$). The droplet shapes obtained in the numerical simulations show an agreeable match with the experimental results. Furthermore, a quantitative comparison in terms of the spreading factor evolution with respect to time is presented in Fig. A.17. The quantitative comparison is also within the agreeable limits.

### *A2. Case 2: Droplet impact over a heated solid surface*

To assess the capability of the solver to simulate the thermal effects in the purview of this problem, a case of droplet impact over a heated solid surface is considered in this section. The numerical setup is made exactly to mimic the study reported by Samkhaniani et al. [56]. Fig. A.18 presents the variation of spreading factor $\beta$ with time for different contact angles. The numerical results match very well with the experimental data through out the droplet impact, spreading, recoiling and bouncing process, for all three contact angles. In addition, numerical predictions of time variation of mean droplet temperature at different values of $We$ is compared with the numerical results of Ref [56], in Fig. A.18b. Present numerical results show very good agreement with the literature data.

### *A3. Case 3: Deformation of a freely suspended dielectric droplet in an external electric field*

This case considers the deformations of a liquid droplet of radius $R_d$ freely suspended in a second liquid exposed to an electric field $E_\infty$ as shown in Fig. 6 of Herrera et al. [44]. The thermophysical properties, dielectric properties and flow configuration, etc. are set exactly same as the case considered in Ref [44]. The radial electric field distribution in polar coordinates for a freely suspended spherical drop in an electric field can be calculated by the following expressions given by Taylor's theory [57].

**Outer fluid**

$$E_{2r} = -\left[1 + \frac{2(K_R - 1)}{2 + K_R}\frac{1}{r^3}\right]\cos\ \theta \tag{A.1}$$

**Inner fluid**

$$E_{1r} = -\frac{3}{2 + K_R}\cos\ \theta \tag{A.2}$$

Fig. A.19a presents a comparison of the present numerical results of radial electric field distribution along $\theta = \pi$ with Eqs. (A.1) and (A.2). Likewise, the axisymmetric velocity profiles $\upsilon_r$ and $\upsilon_\theta$, along $\theta = \pi/4$ is presented in Fig. A.19b. The numerical results are compared with the analytical predictions of Taylor's theory [57] as given by the following expressions:

**Outer fluid**

$$\upsilon_{2r} = A\left(r^{-4} - r^{-2}\right)\left(3\cos^2\theta - 1\right) \text{ and } \upsilon_{2\theta} = -Ar^{-4}\sin\ 2\theta \tag{A.3}$$

**Inner fluid**

$$\upsilon_{1r} = Ar(1 - r^2)(3\cos^2\theta - 1) \text{ and } \upsilon_{1\theta} = \frac{3A}{2}r\left(1 - \frac{5}{3}r^2\right)\sin\ 2\theta \tag{A.4}$$

In all the expressions of Taylor's theory [57], $r$ has been made dimensionless with $R_d$, the normalized electric field is calculated as $E/E_\infty$, the velocity is normalized with the characteristic velocity $\upsilon_c = R_d\varepsilon_2E_\infty^2/\mu_2$. The variable $A$ stands for

$$A = -\frac{9}{10}\frac{R_d\varepsilon_2E_\infty^2}{\mu_2}\frac{1}{(1+\lambda)}\frac{K_R - Q}{(K_R+2)^2} \tag{A.5}$$

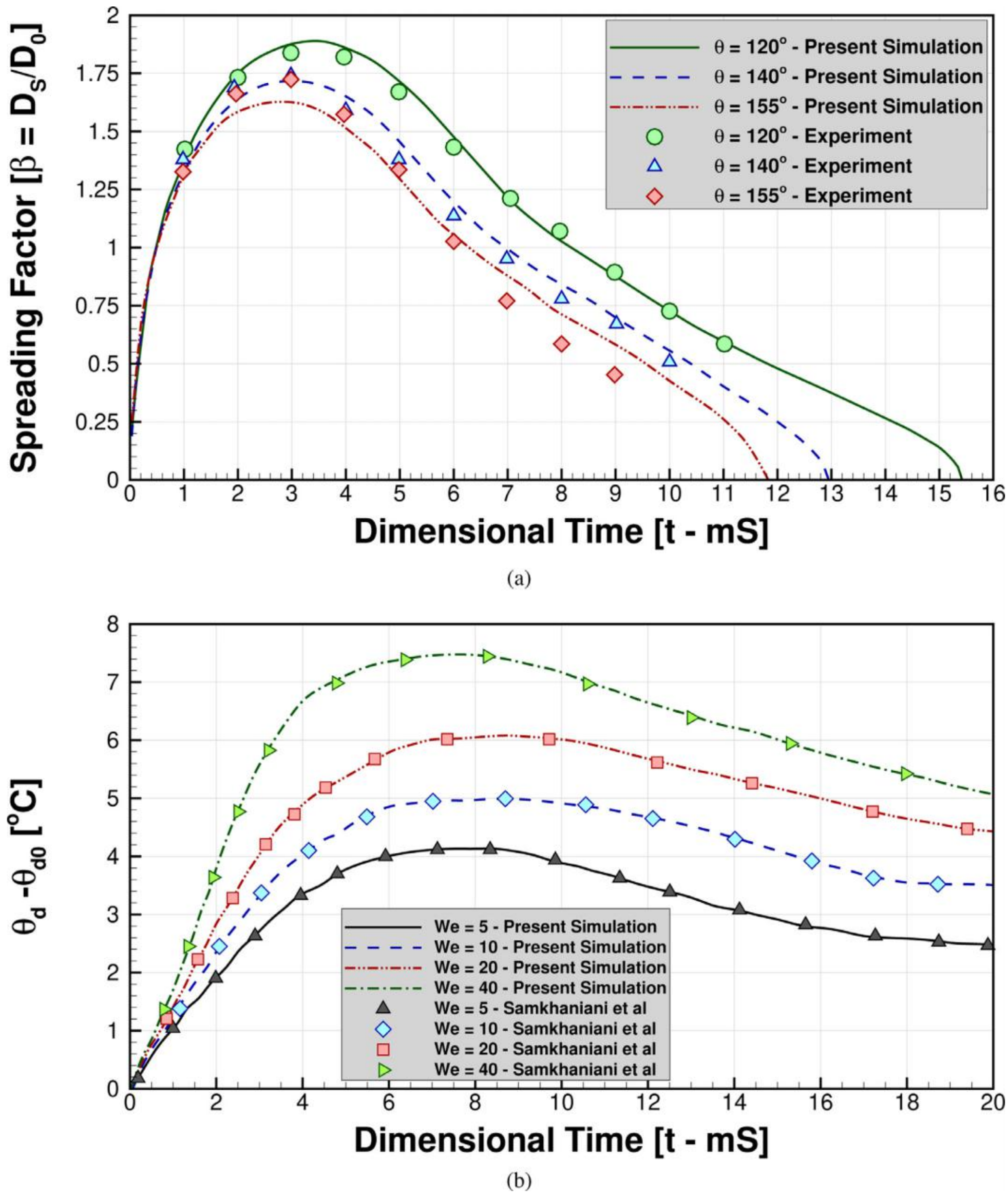


**Fig. A3.** Case 2: Comparison of present numerical results with experimental and numerical results [55,56] for droplet bouncing over a heated solid surface. (*a*) Time evolution of droplet spreading factor ($\beta = D_S/D_0$) for $D_0 = 2.3\,\mathrm{mm}$, $We = 20$, $T_{D,0} = 20^{\circ}C$ and $T_S = 60^{\circ}C$ and (*b*) Droplet mean temperature variation with time ($d_0 = 2.3\,\mathrm{mm}$, $\theta_e = 120^{\circ}$, $T_{d,0} = 20^{\circ}C$, $T_s = 60^{\circ}C$) for impact over a smooth hydrophobic surface ($\theta_e = 120^{\circ}$).

Finally, the total deformation of the droplet characterized by the deformation ratio $D = (b-a)/(a+b)$ at different conductivity ratios $K_R$ and $Ca_E = 0.18$ is presented in Fig. A.19c. The numerical predictions of $D$ is compared with the analytical expression given by Taylor [57], as follows:

$$D = \frac{9}{16}\frac{Ca_E}{(2+K_R)^2}\left[1 + K_R^2 - 2Q + \frac{3}{5}(K_R - Q)\frac{2+3\lambda}{1+\lambda}\right] \tag{A.6}$$

From Fig. A.19, it is clearly seen that the present numerical results show good agreement with the analytical solutions. More importantly, the numerical solver is able to capture the sharp variations across the fluid-fluid interface, without any nonphysical oscillations.

### *A4. Case 4: Impact and bouncing of a droplet over an isothermal hydrophobic surface in an external electric field*

Finally, the case of experimental study of a droplet impact over an isothermal solid surface [32] is considered. The study has reported three different modes at three different electric potentials namely, $7kV$, $7.5kV$ and $8kV$. The temporal evolution of the height ratio ($h_S/h_{S0}$) at the three electric potentials obtained using the present numerical framework is compared with the experimental results in Fig. A.20. Here, $h_S$ is the height of the droplet at instantaneous times and $h_{S0}$ is the height of the droplet at the point of maximum stretching. It is seen that the numerical results match well with the experimental results.

The detailed validation study with respect to experimental, numerical and analytical benchmark results gives us confidence over the results, obtained using the numerical framework utilized in this study.

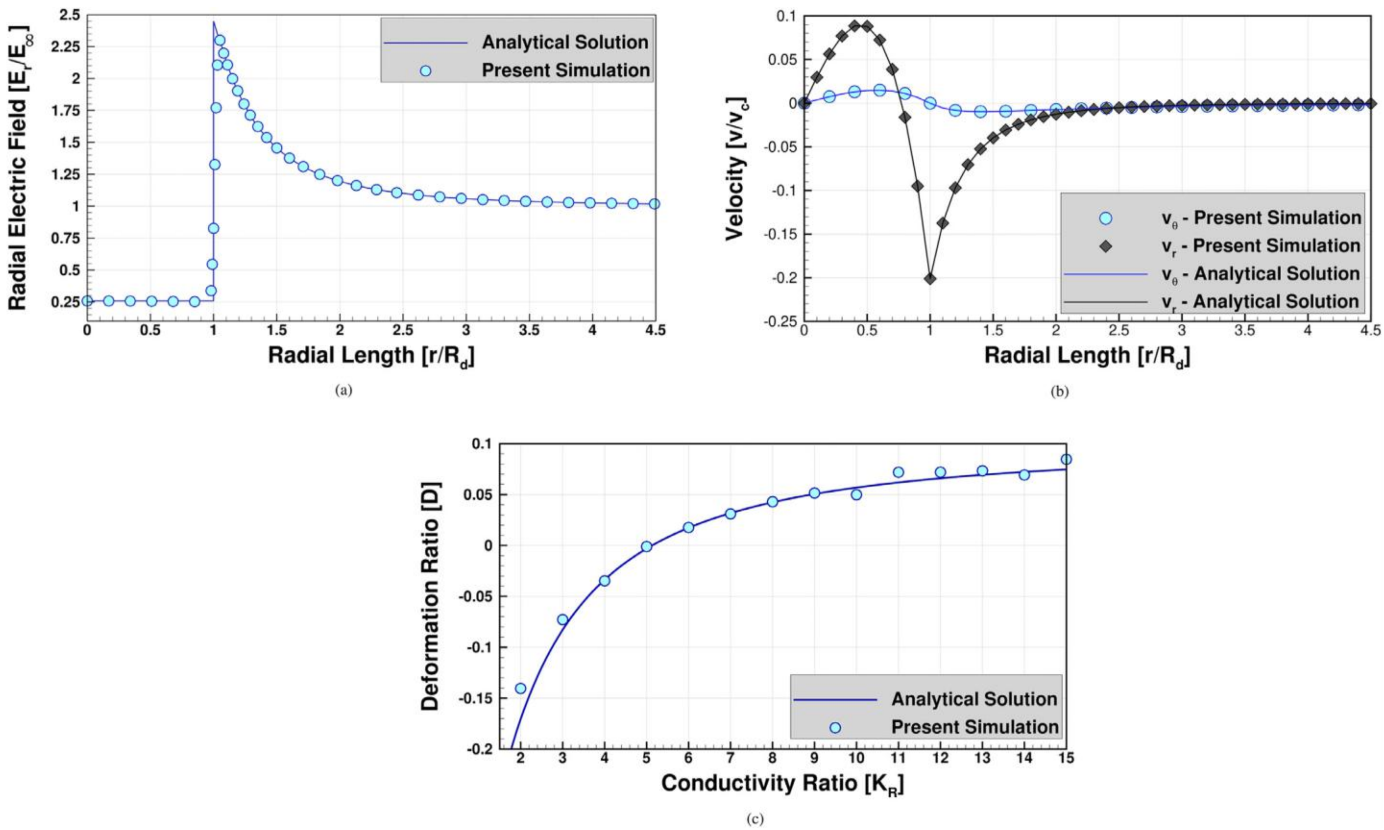


**Fig. A4.** Case 3: Comparison of present numerical results with analytical results [44,57] of deformation of a freely suspended dielectric droplet in an external electric field. (*a*) Radial electric field distribution along angle $\theta = \pi$, (*b*) Velocity components distribution along angle $\theta = \pi/4$ and (*c*) Deformation ratio at different conductivity ratios.

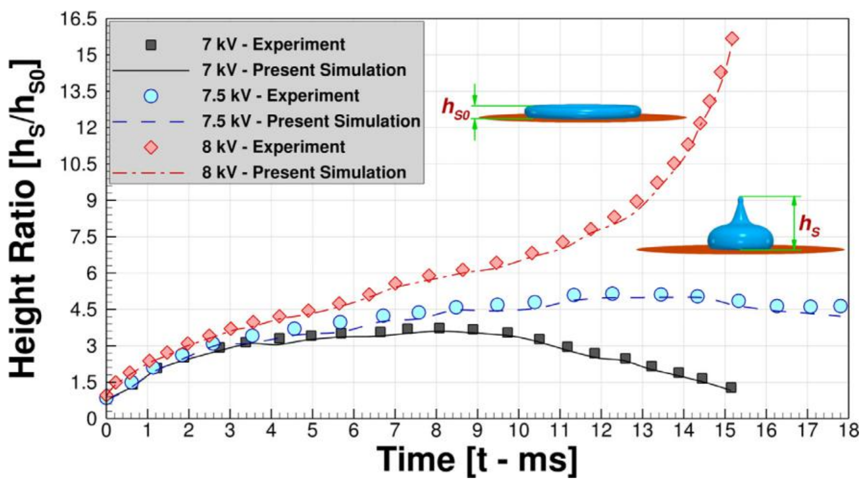


**Fig. A5.** Case 4: Temporal variation of droplet height ratio ($h_S/h_{S0}$) at three different applied electric potential values 7 kV, 7.5 kV and 8 kV. The experimental data is taken from Tian et al. [32].

## References

[1] M. Pasandideh-Fard, S. Aziz, S. Chandra, J. Mostaghimi, Cooling effectiveness of a water drop impinging on a hot surface, Int. J. Heat Fluid Flow 22 (2) (2001) 201–210.
[2] M. Börnhorst, O. Deutschmann, Single droplet impingement of urea water solution on a heated substrate, Int. J. Heat Fluid Flow 69 (2018) 55–61.
[3] G. Liang, I. Mudawar, Review of drop impact on heated walls, Int. J. Heat Mass Transf. 106 (2017) 103–126.
[4] M. Visaria, I. Mudawar, Application of two-phase spray cooling for thermal management of electronic devices, IEEE Trans. Compon. Packag. Technol. 32 (4) (2009) 784–793.
[5] M.H. Mousa, N. Miljkovic, K. Nawaz, Review of heat transfer enhancement techniques for single phase flows, Renewable Sustainable Energy Rev. 137 (2021) 110566.
[6] H.-C. Wang, A.V. Mamishev, Optimal heat transfer performance of the microfluidic electrospray cooling devices, in: 2011 27th Annual IEEE Semiconductor Thermal Measurement and Management Symposium, IEEE, 2011, pp. 35–42.
[7] M. Gibbons, A. Robinson, Heat transfer characteristics of single cone-jet electrosprays, Int. J. Heat Mass Transf. 113 (2017) 70–83.
[8] Y. Kim, S. Jung, S. Kim, S.T. Choi, M. Kim, H. Lee, Heat transfer performance of water-based electrospray cooling, Int. Commun. Heat Mass Transfer 118 (2020) 104861.
[9] E.S. Elton, Y.V. Tibrewala, W.D. Ristenpart, Statistical analysis of droplet charge acquired during contact with electrodes in strong electric fields, Langmuir 35 (11) (2019) 3937–3948.
[10] X. Luo, X. Huang, H. Yan, D. Yang, J. Wang, L. He, Breakup modes and criterion of droplet with surfactant under direct current electric field, Chem. Eng. Res. Des. 132 (2018) 822–830.

[11] D. Sun, F. Cao, L. Cong, W. Xu, Q. Chen, W. Shi, S. Xu, Cellular heterogeneity identified by single-cell alkaline phosphatase (ALP) via a serrs-microfluidic droplet platform, Lab Chip 19 (2) (2019) 335–342.
[12] H. Tavakoli, W. Zhou, L. Ma, S. Perez, A. Ibarra, F. Xu, S. Zhan, X. Li, Recent advances in microfluidic platforms for single-cell analysis in cancer biology, diagnosis and therapy, Trends Anal. Chem. 117 (2019) 13–26.
[13] M.A. Saucedo-Espinosa, P.S. Dittrich, In-droplet electrophoretic separation and enrichment of biomolecules, Anal. Chem. 92 (12) (2020) 8414–8421.
[14] M.J. Divvela, Y.L. Joo, Design principles in continuous inkjet electrohydrodynamic printing from discretized modeling and image analysis, J. Manuf. Process. 54 (2020) 413–419.
[15] T. Leary, M. Yeganeh, C. Maldarelli, Microfluidic study of the electrocoalescence of aqueous droplets in crude oil, ACS Omega 5 (13) (2020) 7348–7360.
[16] M. Abolghasemibizaki, R.L. McMasters, R. Mohammadi, Towards the shortest possible contact time: droplet impact on cylindrical superhydrophobic surfaces structured with macro-scale features, J. Colloid Interface Sci. 521 (2018) 17–23.
[17] M. Abolghasemibizaki, C.J. Robertson, C.P. Fergusson, R.L. McMasters, R. Mohammadi, Rolling viscous drops on a non-wettable surface containing both micro-and macro-scale roughness, Phys. Fluids 30 (2) (2018) 023105.
[18] F. Aouabed, A. Bayadi, R. Boudissa, Flashover voltage of silicone insulating surface covered by water droplets under ac voltage, Electr. Power Syst. Res. 143 (2017) 66–72.
[19] Y. Li, Y. Mu, S. Yuan, L. Guo, The game theoretical approach for multi-phase complex systems in chemical engineering, J. Syst. Sci. Complex. 30 (1) (2017) 4–19.
[20] Y. Yang, X. Tan, D. Liu, X. Lu, C. Zhao, J. Lu, Y. Pan, Corona discharge-induced rain and snow formation in air, IEEE Trans. Plasma Sci. 46 (5) (2018) 1786–1792.
[21] Y. Zhu, M. Otsubo, C. Honda, S. Tanaka, Corona discharge from water droplet on electrically stressed polymer surface, Jpn. J. Appl. Phys. 45 (1R) (2006) 234.
[22] B. Khorshidi, M. Jalaal, E. Esmaeilzadeh, F. Mohammadi, Characteristics of deformation and electrical charging of large water drops immersed in an insulating liquid on the electrode surface, J. Colloid Interface Sci. 352 (1) (2010) 211–220.
[23] D.J. Im, M.M. Ahn, B.S. Yoo, D. Moon, D.W. Lee, I.S. Kang, Discrete electrostatic charge transfer by the electrophoresis of a charged droplet in a dielectric liquid, Langmuir 28 (32) (2012) 11656–11661.
[24] E. Bormashenko, R. Pogreb, T. Stein, G. Whyman, M. Schiffer, D. Aurbach, Electrically deformable liquid marbles, J. Adhes. Sci. Technol. 25 (12) (2011) 1371–1377.
[25] E. Bormashenko, R. Pogreb, T. Stein, G. Whyman, M. Hakham-Itzhaq, Electrostatically driven droplets deposited on superhydrophobic surfaces, Appl. Phys. Lett. 95 (26) (2009) 264102.
[26] K.J. Bishop, A.M. Drews, C.A. Cartier, S. Pandey, Y. Dou, Contact charge electrophoresis: fundamentals and microfluidic applications, Langmuir 34 (22) (2018) 6315–6327.
[27] S.U. Ryu, S.Y. Lee, Maximum spreading of electrically charged droplets impacting on dielectric substrates, Int. J. Multiphase Flow 35 (1) (2009) 1–7.
[28] S. Pal, A.M. Miqdad, S. Datta, A.K. Das, P.K. Das, Control of drop impact and proposal of pseudo-superhydrophobicity using electrostatics, Industr. Eng. Chem. Res. 56 (39) (2017) 11312–11319.
[29] V. Yurkiv, A.L. Yarin, F. Mashayek, Modeling of droplet impact onto polarized and nonpolarized dielectric surfaces, Langmuir 34 (34) (2018) 10169–10180.
[30] M. Emdadi, P. Pournaderi, Numerical simulation of conducting droplet impact on a surface under an electric field, Acta Mech. 231 (3) (2020) 1083–1103.
[31] H. Dastourani, M. Jahannama, A. Eslami-Majd, A physical insight into electrospray process in cone-jet mode: role of operating parameters, Int. J. Heat Fluid Flow 70 (2018) 315–335.
[32] Y. Tian, H. Wang, X. Zhou, Q. Deng, X. Zhu, R. Chen, Y. Ding, Q. Liao, A combined experimental and numerical study on droplet-impact induced breakup and ejection behaviors in vertical electric field, Chem. Eng. Sci. 239 (2021) 116636.
[33] J.L. Lara, F. Pontiga, A. Castellanos, Stability analysis of a taylor–couette flow of insulating fluid subjected to radial unipolar injection of charge, Phys. Fluids 10 (12) (1998) 3088–3098.
[34] J. Wu, P. Traoré, A finite-volume method for electro-thermoconvective phenomena in a plane layer of dielectric liquid, Numer. Heat Transfer, Part A 68 (5) (2015) 471–500.
[35] J. Hua, L.K. Lim, C.-H. Wang, Numerical simulation of deformation/motion of a drop suspended in viscous liquids under influence of steady electric fields, Phys. Fluids 20 (11) (2008) 113302.
[36] M. Sussman, E. Fatemi, P. Smereka, S. Osher, An improved level set method for incompressible two-phase flows, Comput. Fluids 27 (5–6) (1998) 663–680.
[37] E. Bjørklund, The level-set method applied to droplet dynamics in the presence of an electric field, Comput. Fluids 38 (2) (2009) 358–369.
[38] A. Albadawi, D. Donoghue, A. Robinson, D. Murray, Y. Delauré, Influence of surface tension implementation in volume of fluid and coupled volume of fluid with level set methods for bubble growth and detachment, Int. J. Multiphase Flow 53 (2013) 11–28.
[39] J.U. Brackbill, D.B. Kothe, C. Zemach, A continuum method for modeling surface tension, J. Comput. Phys. 100 (2) (1992) 335–354.
[40] A. Castellanos, Electrohydrodynamics, volume 380, Springer Science & Business Media, 1998.
[41] E. Murphy, Dielectric breakdown, in: Digest of Literature on Dielectrics, volume 11, IEEE, 1947, pp. 40–48.
[42] C. SatyanarayanaRaju, C.V. Krishnamurthy, Charge migration model for the impedance response of di water, AIP Adv. 9 (3) (2019) 035141.
[43] D. Saville, Electrohydrodynamics: the taylor-melcher leaky dielectric model, Annu. Rev. Fluid Mech. 29 (1) (1997) 27–64.
[44] J. López-Herrera, S. Popinet, M. Herrada, A charge-conservative approach for simulating electrohydrodynamic two-phase flows using volume-of-fluid, J. Comput. Phys. 230 (5) (2011) 1939–1955.
[45] D. Fleisch, A student's guide to Maxwell's equations, Cambridge University Press, 2008.
[46] F. Almasi, M.S. Shadloo, A. Hadjadj, M. Ozbulut, N. Tofighi, M. Yildiz, Numerical simulations of multi-phase electro-hydrodynamics flows using a simple incompressible smoothed particle hydrodynamics method, Comput. Math. Appl. 81 (2021) 772–785.
[47] S. Santra, S. Mandal, S. Chakraborty, Electrohydrodynamics of confined two-dimensional liquid droplets in uniform electric field, Phys. Fluids 30 (6) (2018) 062003.
[48] S. Torza, R. Cox, S. Mason, Electrohydrodynamic deformation and bursts of liquid drops, Philos. Trans. R. Soc. Lond. Ser. A Math. Phys. Sci. 269 (1198) (1971) 295–319.
[49] G. Tomar, D. Gerlach, G. Biswas, N. Alleborn, A. Sharma, F. Durst, S.W. Welch, A. Delgado, Two-phase electrohydrodynamic simulations using a volume-of-fluid approach, J. Comput. Phys. 227 (2) (2007) 1267–1285.
[50] W. Li, J. Wang, C. Zhu, L. Tian, N. Zhao, Numerical investigation of droplet impact on a solid superhydrophobic surface, Phys. Fluids 33 (6) (2021) 063310.
[51] F. Moukalled, L. Mangani, M. Darwish, et al., The finite volume method in computational fluid dynamics, An advanced introduction with OpenFoam® and Matlab®. Nueva York: Springer. Recuperado de http://www. gidropraktikum. narod. ru/Moukalled-et-al-FVM-OpenFOAM-Matlab. pdf (2016).
[52] B.P. Leonard, A stable and accurate convective modelling procedure based on quadratic upstream interpolation, Comput. Methods Appl. Mech. Eng. 19 (1) (1979) 59–98.
[53] B. Van Leer, Towards the ultimate conservative difference scheme, J. Comput. Phys. 135 (2) (1997) 229–248.
[54] T. Holzmann, Mathematics, numerics, derivations and openfoam®, Loeben, Germany: Holzmann CFD (2016).
[55] C. Guo, D. Maynes, J. Crockett, D. Zhao, Heat transfer to bouncing droplets on superhydrophobic surfaces, Int. J. Heat Mass Transf. 137 (2019) 857–867.
[56] N. Samkhaniani, A. Stroh, M. Holzinger, H. Marschall, B. Frohnapfel, M. Wörner, Bouncing drop impingement on heated hydrophobic surfaces, Int. J. Heat Mass Transf. 180 (2021) 121777.
[57] G.I. Taylor, Studies in electrohydrodynamics. I. The circulation produced in a drop by an electric field, Proc. R. Soc. Lond. Ser. A. Math. Phys. Sci. 291 (1425) (1966) 159–166.